

LA-10202-MS

2.3

CIC-14 REPORT COLLECTION
**REPRODUCTION
COPY**

Los Alamos National Laboratory is operated by the University of California for the United States Department of Energy under contract W-7405-ENG-36

*The Thermal Conductivity
of an Arbitrarily Dense Plasma*

LOS ALAMOS NATIONAL LABORATORY



3 9338 00318 6227

Los Alamos Los Alamos National Laboratory
Los Alamos, New Mexico 87545

DISCLAIMER

This report was prepared as an account of work sponsored by an agency of the United States Government. Neither the United States Government nor any agency thereof, nor any of their employees, makes any warranty, express or implied, or assumes any legal liability or responsibility for the accuracy, completeness, or usefulness of any information, apparatus, product, or process disclosed, or represents that its use would not infringe privately owned rights. Reference herein to any specific commercial product, process, or service by trade name, trademark, manufacturer, or otherwise, does not necessarily constitute or imply its endorsement, recommendation, or favoring by the United States Government or any agency thereof. The views and opinions of authors expressed herein do not necessarily state or reflect those of the United States Government or any agency thereof.

LA-10202-MS

UC-34

Issued: October 1984

The Thermal Conductivity of an Arbitrarily Dense Plasma



George Rinker



Los Alamos Los Alamos National Laboratory
Los Alamos, New Mexico 87545

THE THERMAL CONDUCTIVITY OF AN ARBITRARILY DENSE PLASMA

by
George Rinker

ABSTRACT

This is the second in a series of reports concerning the transport properties of dense plasmas. In this work, we use the formalism of Lampe to extend our previous calculations of electrical conductivity to the calculation of thermal conductivity and thermoelectric coefficient. Quantitative results are given for iron at temperatures ranging from 10^{-2} to 10^4 eV and for densities from 3×10^{-4} to 10^5 g/cm³.

Lampe [1968] has calculated electrical and thermal transport coefficients for a weakly-coupled plasma with any degree of electron degeneracy. His calculation is carried out by solving the Lenard-Balescu equation by the Chapman-Enskog method, using Fermi-statistical generalizations of the first two Sonine polynomials.

The physical models he incorporates for the electron-ion and electron-electron interactions are ultimately expressed by Coulomb logarithms. These are calculated using Born approximation with Debye-shielded potentials. The requirement of weak coupling arises principally from his use of Born approximation for the electron-ion scattering cross section and neglect of lattice structure at high density.

In a previous report [Rinker 1984], we described a method for the complete partial-wave analysis of the Ziman formula for the electrical resistivity, using self-consistent ionic potentials, realistic structure factors, and arbitrary electron degeneracy. Our calculations thus avoid the shortcomings of Born approximation and are valid for much stronger electron-ion couplings. We use an approximate scheme to compensate for multiple-scattering effects and density fluctuations. The validity of this scheme is unknown, but we have obtained good

agreement for liquid metals near the melting point. In fact, our calculations generally do as well as theoretical pseudopotential models and are surpassed only by those pseudopotential calculations that are highly parametrized to reproduce known conduction-band data.

Boercker et al. [1982] have shown that with appropriate choices for the structure factor, the Ziman formula and the Lenard-Balescu equation are equivalent in the weak-coupling limit. In the present work, we exploit this fact by combining our electrical conductivity calculations with the formal results of Lampe to obtain improved thermal transport coefficients. In our approach, we simply replace Lampe's expression for the electron-ion Coulomb logarithm with a numerical value that is adjusted to reproduce our calculated electrical conductivity. We do not modify his expression for the electron-electron Coulomb logarithm, as we expect Born approximation to be valid in that case for virtually all conditions. Thus we obtain an internally consistent set of calculations for the ionization state, electrical conductivity, thermal conductivity, and thermoelectric coefficient. We expect these calculations to have a wider range of validity in temperature and density than previous calculations.

Lampe's coefficients are defined with respect to the transport equations

$$\begin{aligned} \underline{J} &= eS_{11}\left(e\underline{E} + \frac{\nabla P}{n_e}\right) + eS_{12} \frac{\nabla T}{T} \\ \underline{Q} &= -S_{21}\left(e\underline{E} + \frac{\nabla P}{n_e}\right) - S_{22} \frac{\nabla T}{T} + \frac{5}{3} \left(\frac{\underline{J}}{e}\right)\epsilon \end{aligned}$$

where

\underline{J} = electric current

e = electron charge

\underline{E} = applied electric field

$$P = \frac{2}{3} n_e \epsilon + kT \frac{n_e}{Z} = \text{pressure}$$

n_e = electron number density

T = temperature

Q = heat flux

ϵ = mean kinetic energy per electron.

The electrical conductivity σ and thermal conductivity κ (with the conventional constraint $J=0$) are

$$\sigma = e^2 S_{11}$$

$$\kappa = (S_{11}S_{22} - S_{12}^2)/(TS_{11}) .$$

The quantity $S_{12}=S_{21}$ will be called the thermoelectric coefficient.

Lampe's explicit expressions for S_{ij} are rather lengthy and will not be reproduced here. In addition to the Coulomb logarithms, they involve generalized Fermi-Dirac integrals, which account for the electron statistics. Accurate expressions for these integrals have not been available previously. For the present application, Fullerton [1982] has obtained highly efficient 10-decimal Chebyshev approximations. These approximations are effective except in cases of extreme electron degeneracy ($\mu/kT > 10^4$, where μ is the chemical potential). The approximations fail because Lampe's expressions contain combinations of the functions that ultimately become numerically unstable. These combinations include terms with as many as 5 factors of the integrals to be evaluated. Each integral has an asymptotic expansion of the form

$$I_k(z) \underset{z \rightarrow \infty}{\sim} z^k \sum_{i=0}^{\infty} a_i z^{-i} .$$

where $z = \mu/kT$ is the degeneracy parameter. The instabilities arise through

cancellation of the leading terms in z . In principle, the expansions and series manipulations can be done analytically to extract the surviving terms. Instead, we have chosen the easier and equivalent method of simply evaluating Fullerton's approximations, combining them, and determining the asymptotic coefficients numerically before instability sets in.

As an example of the application of this procedure, we consider the computation of the remaining transport coefficients from our previous results for the ionization state and electrical conductivity of iron at various temperatures and densities [Rinker 1984]. Figures 1-8 show numerically computed values for temperatures and densities on a logarithmic grid. Temperatures range from 10^{-2} to 10^4 eV, and densities range from 3×10^{-4} to 10^5 g/cm³. Figure 1 shows the ionization state Z_i as a three-dimensional surface, and Fig. 2 shows the same data as a contour plot. At very low densities, the ionization state approaches zero as $kT \rightarrow 0$ because sufficient bound states are formed to accommodate all electrons. The onset of thermal ionization as kT increases and of pressure ionization as p increases is readily apparent. Surface irregularities arise from shell structure in the partial-wave analysis. The transport coefficients are strongly coupled to these ionization states in the present model.

Figures 3 and 4 show the electrical conductivity σ in the units s^{-1} . The sharp peak near normal density at small kT arises from the ionization of the 4s and 3d states and the strong d-wave scattering, which makes iron a transition metal. In other regions of p and kT , the behavior of its electrical conductivity is more nearly normal.

Virtually no experimental conductivity data exist in the regions of temperature and density for which our model is strictly applicable. The only clear point of comparison is the electrical resistivity of the liquid at melting point. Here our model gives the surprisingly good result of 118 $\mu\Omega \cdot \text{cm}$, compared with the experimental value of 138.6. This good agreement is satisfying but probably not physically significant, as experience with other elements indicates probable errors of at least a factor of 2 in the model. Table I gives additional comparisons for the solid phase at room temperature and at the melting point. The inapplicability of the model for the solid phase is readily

apparent. The calculated temperature dependence is negligible, whereas experimentally, the resistivity decreases dramatically as the temperature is decreased. This presumably arises from additional transport processes not considered here.

Figures 5 and 6 show the thermal conductivity κ in units $\text{cm}^{-1}\text{s}^{-1}$. The transition-metal peak in the electrical conductivity is smaller in relative magnitude because of the additional process of electron-electron scattering, which does not contribute to the electrical conductivity. Table II gives comparisons with experimental measurements for the solid phase. As with the electrical conductivity, the agreement is good near the melting point but deteriorates as the temperature is lowered. The experimental values decrease with temperature at first but then rise as additional transport processes become active, whereas the calculated values decrease monotonically. Experimental measurements are not available for the liquid phase.

=====

Table I
 Comparison of calculated electrical resistivity η_c ($\mu\Omega\cdot\text{cm}$)
 and experimental resistivity η_x for solid and liquid iron

Phase	ρ (g/cm^3)	T (K)	η_c	η_x	$\frac{1}{\eta_c} \frac{d\eta_c}{dT}$	$\frac{1}{\eta_x} \frac{d\eta_x}{dT}$
Solid	7.86	293	135	9.7 ^a	1.3×10^{-5}	6.5×10^{-3}
Solid	7.36	1810	126	127.5 ^b	1.1×10^{-5}	...
Liquid	7.05	1810	118	138.6 ^b	1.0×10^{-5}	2.4×10^{-4}

^aWeast [1983a].

^bWilson [1965].

=====

Table II
 Comparison of calculated thermal conductivity κ_c (erg \cdot K $^{-1}$ s $^{-1}$ cm $^{-1}$)
 and experimental conductivity κ_x for solid iron at zero pressure

ρ (g/cm 3)	T (K)	κ_c	κ_x (a)
7.86	300	0.55×10^6	8.03×10^6
7.76	600	1.10×10^6	5.47×10^6
7.66	900	1.68×10^6	3.80×10^6
7.56	1200	2.26×10^6	2.82×10^6
7.46	1500	2.86×10^6	3.18×10^6

^aWeast [1983b].

Figures 7 and 8 show the thermoelectric coefficient S_{12} in cm $^{-1}$ s $^{-1}$.
 Figures 9 and 10 show the conductive opacity κ_e in cm 2 g $^{-1}$. This quantity is
 related simply to the thermal conductivity by

$$\kappa_e = \frac{16}{3} \frac{\sigma_{sb}}{k} \frac{T^3}{\rho \kappa} .$$

where

$$\sigma_{sb}/k = 4.10696 \times 10^{11} \text{ s}^{-1} \text{ cm}^{-2} \text{ K}^{-3} .$$

It is included here for convenient comparison with radiative opacities.

Figures 11 and 12 show a comparison of the Hubbard and Lampe [1969] electrical conductivity calculations with our work. Plotted is the ratio of our result to theirs, where in both cases the ionization states displayed in Figs. 1 and 2 are assumed. In the regions of temperature and density where this ratio is set to 10^{-2} , Hubbard and Lampe do not consider their calculation to be valid. The ratio varies between 1/2 and 2 throughout most of the region of high temperature and low density. The fact that it is not uniformly 1 apparently arises from errors in Born approximation and differences in the structure factor.

Figures 13-18 give comparisons with the Lorentz gas model, which neglects electron-electron contributions to thermal conduction and yields the simple relationships

$$\kappa = \frac{4kT}{\omega^2 c} \sigma$$

and

$$S_{12} = \frac{3}{8} \kappa .$$

Figures 13 and 14 show the ratio of the thermal conductivity to the Lorentz gas result. Deviation from 1 in this ratio indicates the importance of electron-electron collisions. These are important at intermediate temperature and low density. Figures 15 and 16 show the same for the thermoelectric coefficient. In addition to the above region of importance, very large deviations occur in regions of high degeneracy (low temperature and high density). Figures 17 and 18 show the ratio $8S_{12}/3\kappa$, which is identically 1 in the Lorentz gas model. Large deviations occur for high degeneracy.

Figures 19 and 20 display the degeneracy parameter μ/kT . The dramatic change from a nondegenerate system to a degenerate system at high density and low temperature is readily apparent.

The ion-ion coupling constant

$$\Gamma = \frac{Z_i^2 e^2 n_c}{k T R_t}$$

is plotted in Figs. 21 and 22. One-component plasma calculations indicate crystallization at $\Gamma=170$ for any material. A rough semiempirical check on this value is given by evaluating our model at the zero-pressure melting temperature. Values at the experimental solid and liquid densities are $\Gamma=204$ and 190, respectively. On the scale of the figures, differences between these values of Γ are hardly visible. The heavy line on Fig. 22 at $\log\Gamma=2.25$ indicates this phase transition.

Figures 23 and 24 show the plasma frequency

$$\left(\frac{\hbar\omega_p}{kT}\right)^2 = \frac{3(\hbar c)^2}{k T R_t^2 M_N c^2} \Gamma$$

where M_N is the nuclear mass.

Figures 25 and 26 show the ionic Debye radius

$$\frac{R_d}{R_t} = (3\Gamma)^{-1/2}$$

This parameter becomes too small to be meaningful well inside the solid-phase region.

In Figs. 27 and 28, we interpret from the values given in Figs. 1-4 a classical mean free path λ , defined by

$$\frac{\lambda}{R_t} = \frac{4\pi}{3} \langle p \rangle \frac{R_t^2}{Z_i \alpha c} \sigma .$$

The quantity $\langle p \rangle$ is a suitable average value for the electron momentum and is equal to the Fermi momentum p_F at high degeneracy. The effects of shell structure are dramatic at low temperature near the metal-insulator transition, as would be expected. At low temperature and density (insulating phase), this parameter becomes completely meaningless.

Figure 29 is a contour plot of the free electron number density per unit volume.

We expect the present results to be reliable throughout the region $\Gamma < 200$ (see Fig. 22). They should be particularly useful because they extend the region of feasible calculation well beyond the limits imposed by Born approximation [compare Figs. 12 and 22; see also Itoh et al. 1983, Mitake et al. 1984].

Difficulties are encountered near the metal-insulator phase transition at low temperature. These difficulties arise from the sensitivity of our results to ionic shell structure. This shell structure can be adjusted within limits by altering the potentials used, but great significance cannot be attached to the results. In reality, the problem in this region of temperature and density involves the interaction of a great many degrees of freedom in the absence of long-range order and is so far not amenable to accurate solution.

Further difficulties arise for $\Gamma > 200$. In this region crystallization occurs, and it is clear (see Tables I and II) that our approach quickly becomes inadequate as the crystal becomes more tightly bound in relation to the temperature. Some efforts have been made to account for these effects in a systematic way [Hubbard and Lampe 1969, Lee and More 1983, Itoh et al. 1984]. We have investigated purely empirical adjustment schemes to force our results to

fit solid-state experimental data. It is not particularly difficult to produce accurate fits, but whether extrapolation of these fits into experimentally unavailable regions can be expected to make sense remains to be seen.

ACKNOWLEDGMENT

I would like to thank L. W. Fullerton for inventing and providing me with routines to calculate the generalized Fermi-Dirac integrals.

REFERENCES

- Boercker, D. B., F. J. Rogers, and H. E. DeWitt. 1982. Phys. Rev. A25, 1623.
- Fullerton, L. W., 1982. Numerical Techniques for Generalized Fermi-Dirac Integrals (Coyote Press, Velarde, NM).
- Hubbard, W. B., and M. Lampe. 1969. Astrophys. J. Suppl. Ser. 18, 297.
- Itoh, N., S. Mitake, H. Iyetomi, and S. Ichimaru. 1983. Astrophys. J. 273, 774.
- Itoh, N., Y. Kohyama, N. Matsumoto, and M. Seki, 1984. "Electrical and Thermal Conductivities of Dense Matter in the Crystalline Lattice Phase." (to be published in Astrophys. J.)
- Lampe, M., 1968. Phys. Rev. 174, 276.
- Lee, Y. T., and R. M. More. 1983. Phys. Fluids 27, 1273.
- Mitake, S., S. Ichimaru, and N. Itoh. 1984. Astrophys. J. 277, 375.
- Rinker, G. A., 1984. "The Electrical Conductivity of an Arbitrarily Dense Plasma." Los Alamos National Laboratory report LA-9872-MS (January 1984).
- Weast, R. C., ed., 1983a. CRC Handbook of Chemistry and Physics. (CRC Press, Boca Raton, Florida), p. F-125.
- Weast, R. C., ed., 1983b. CRC Handbook of Chemistry and Physics. (CRC Press, Boca Raton, Florida), p. E-9.
- Wilson, J. R., 1965. Metall. Rev. 10, 381.

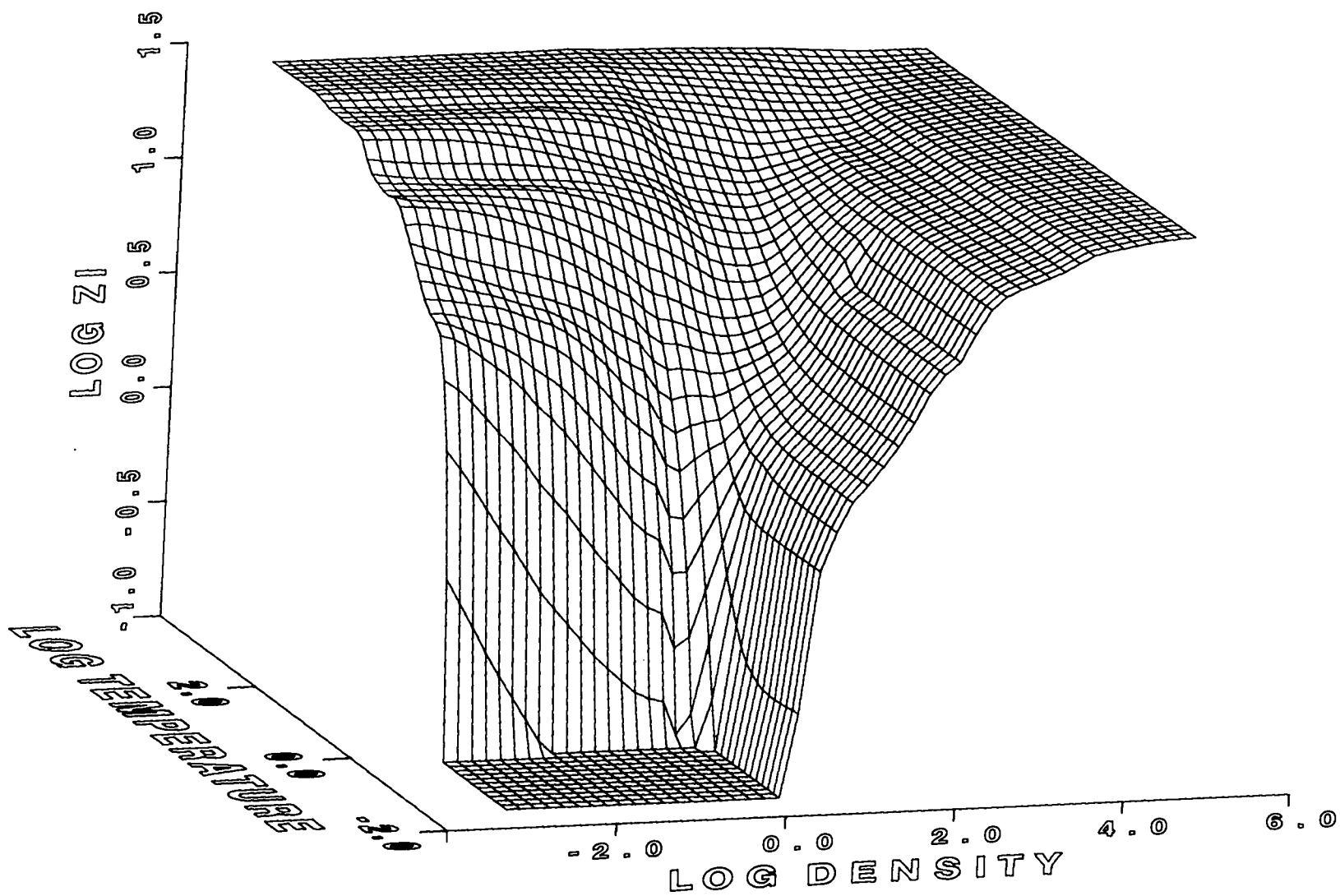


FIG. 1. Ionization states.

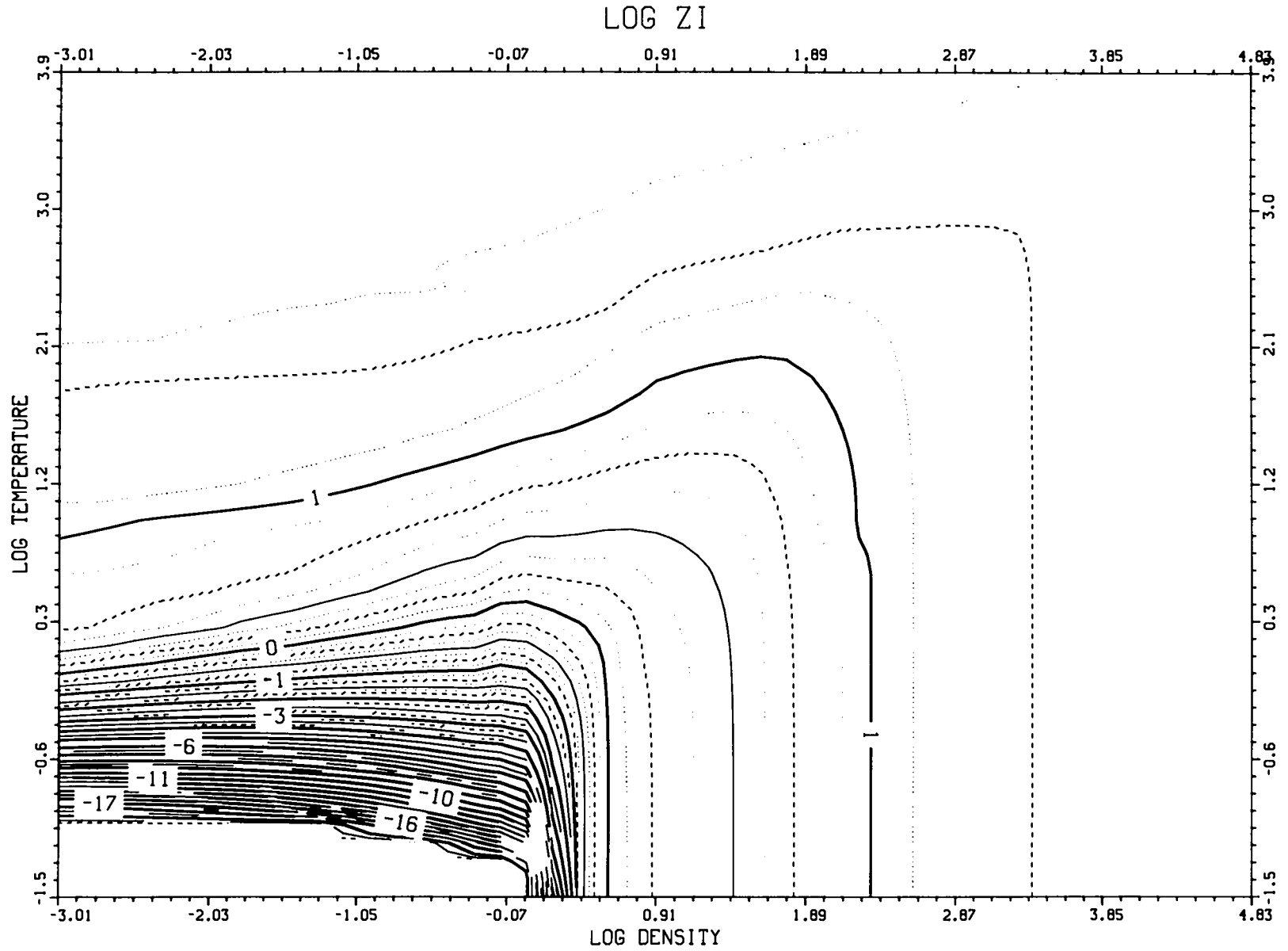


FIG. 2. Ionization states.

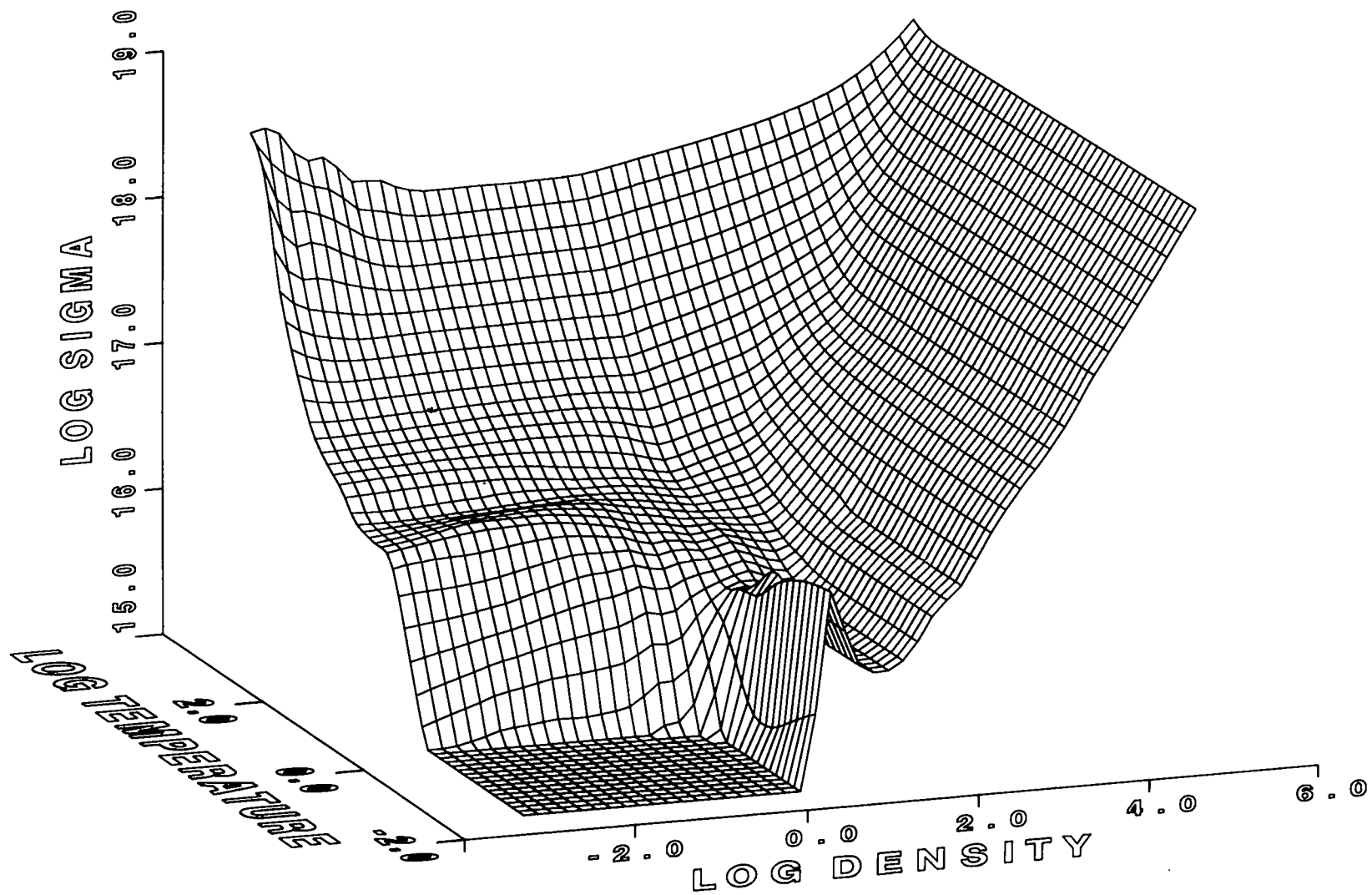


FIG. 3. Electrical conductivity (s^{-1}).

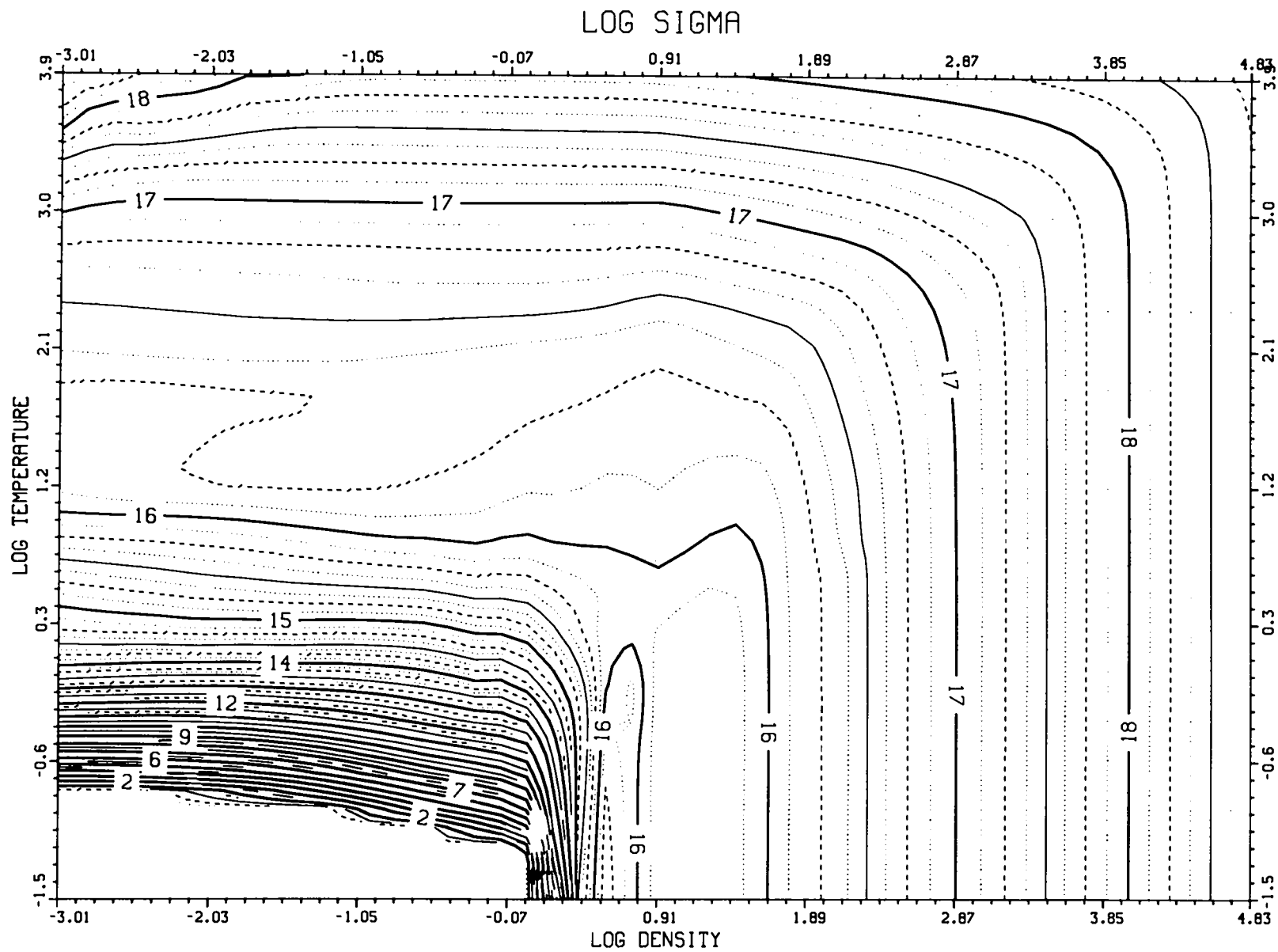


FIG. 4. Electrical conductivity (s^{-1}).

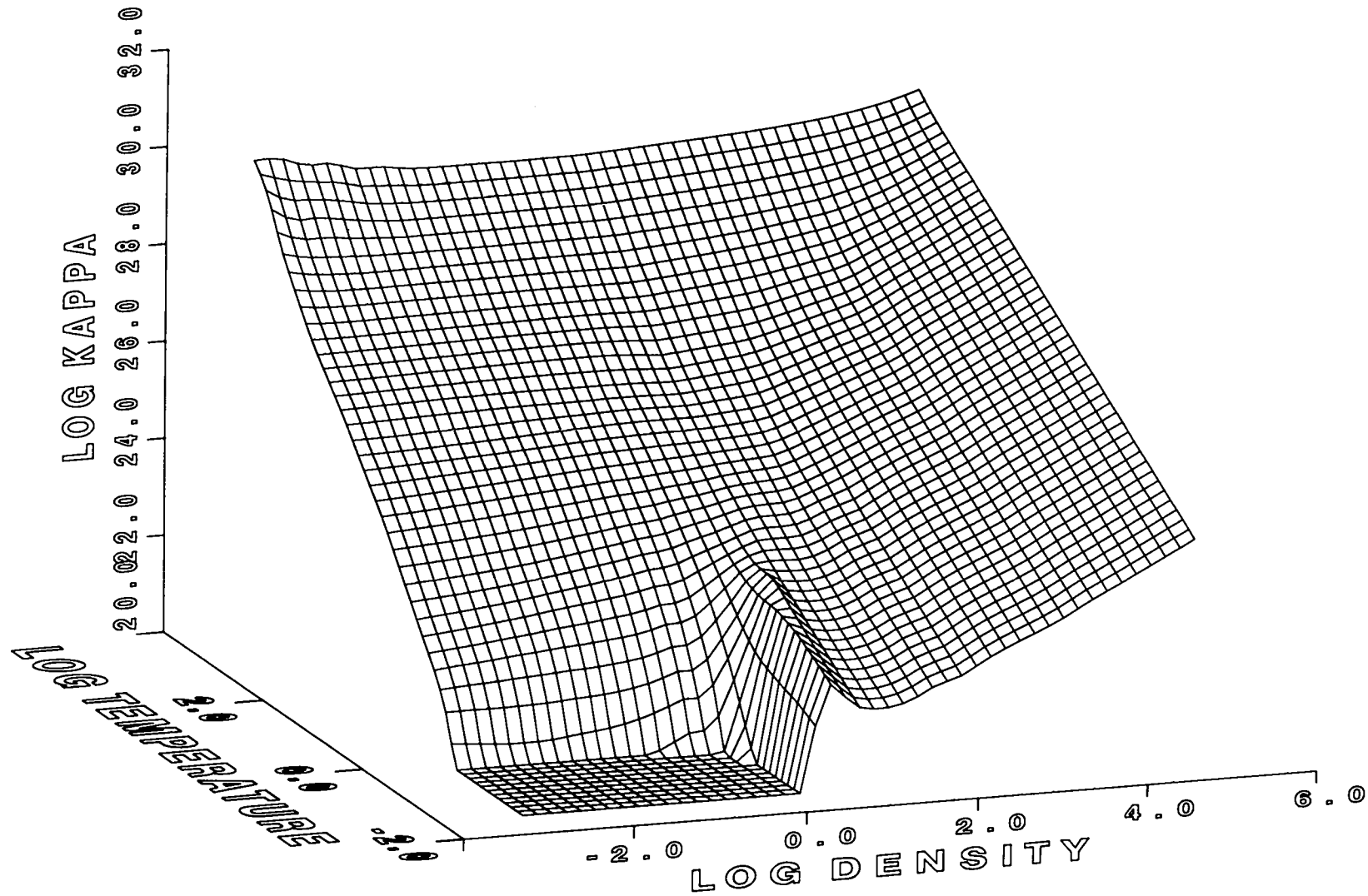


FIG. 5. Thermal conductivity ($\text{cm}^{-1}\text{s}^{-1}$).

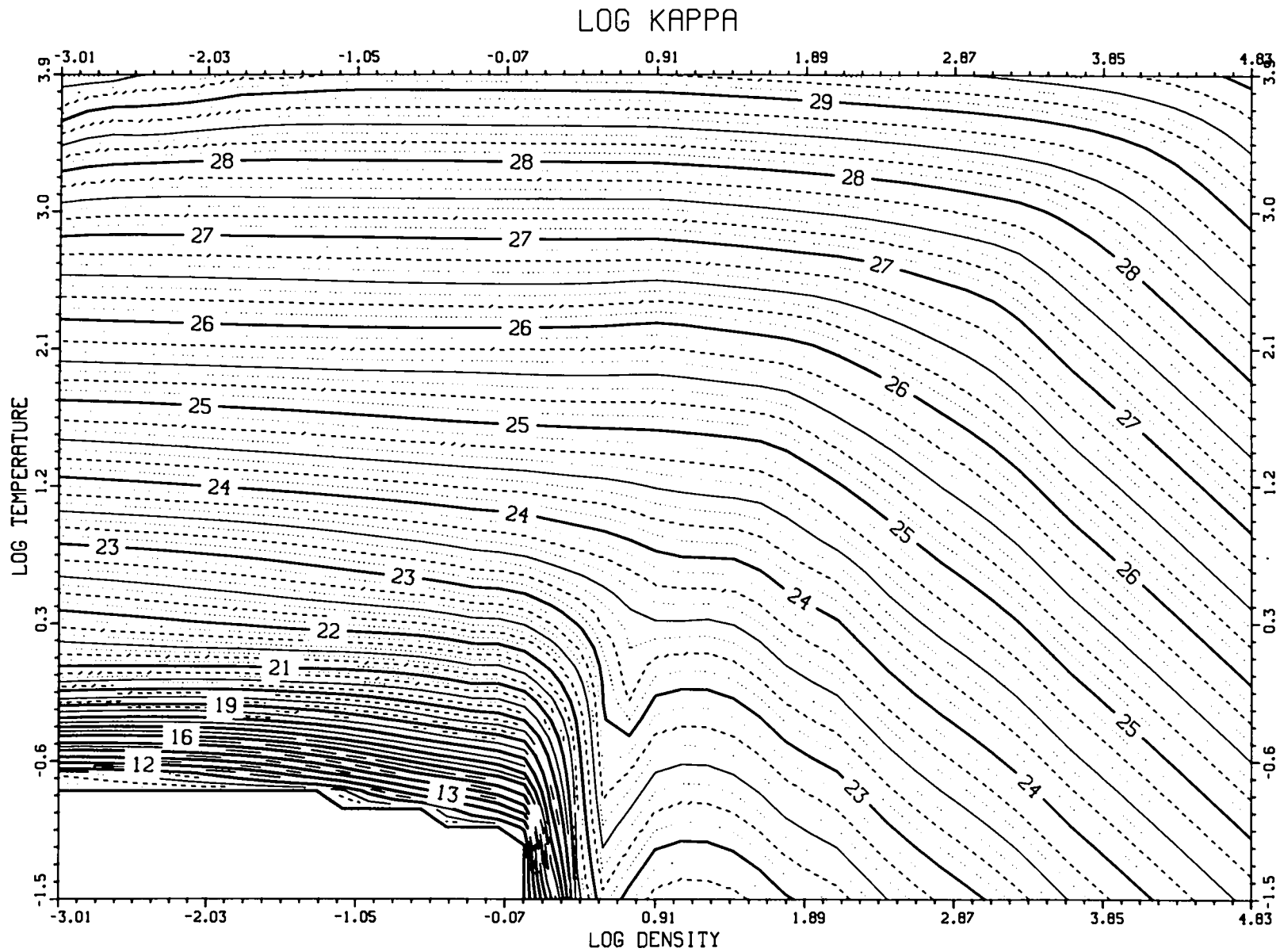


FIG. 6. Thermal conductivity ($\text{cm}^{-1}\text{s}^{-1}$).

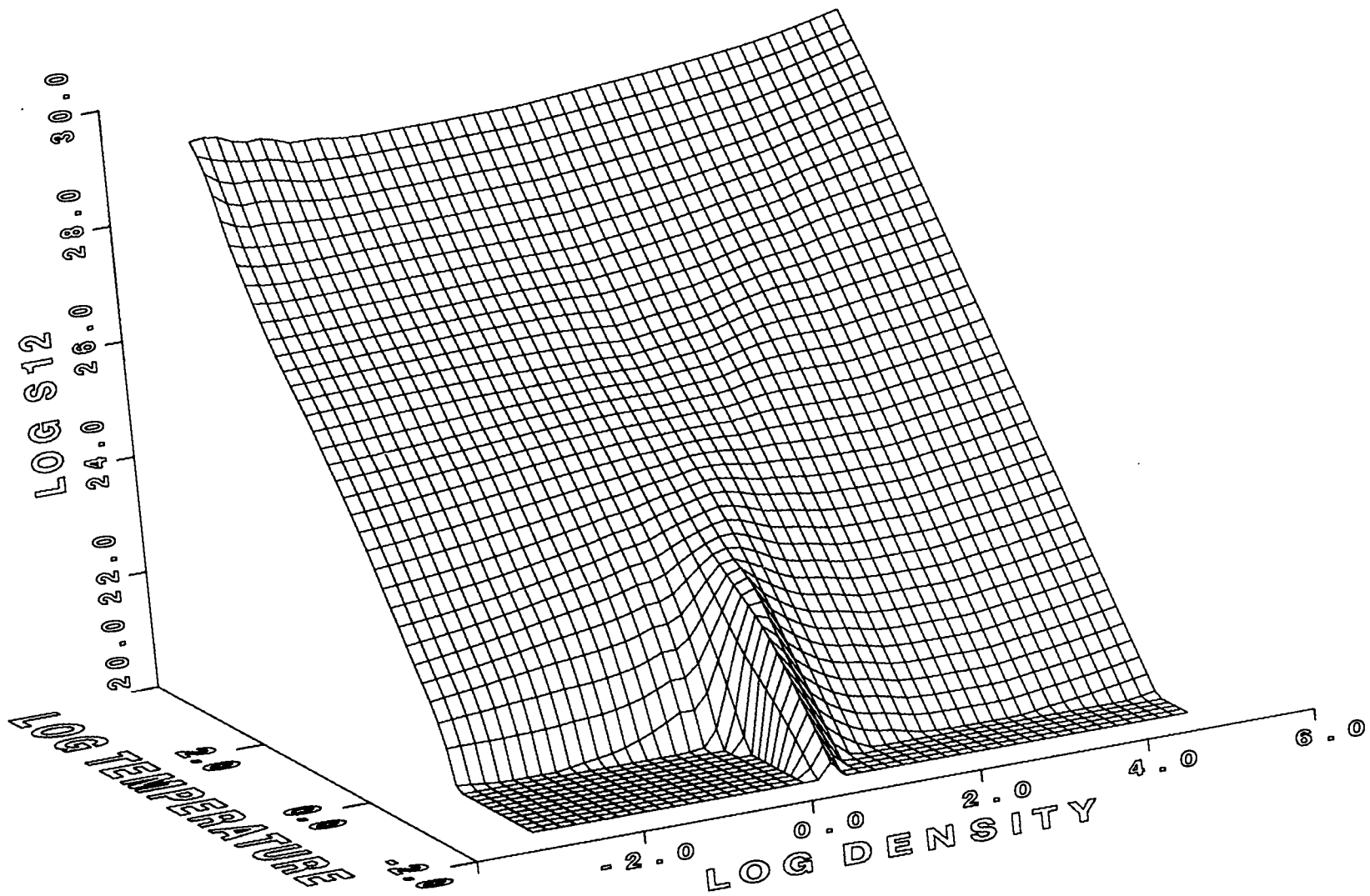


FIG. 7. Thermoelectric coefficient (cm⁻¹s⁻¹).

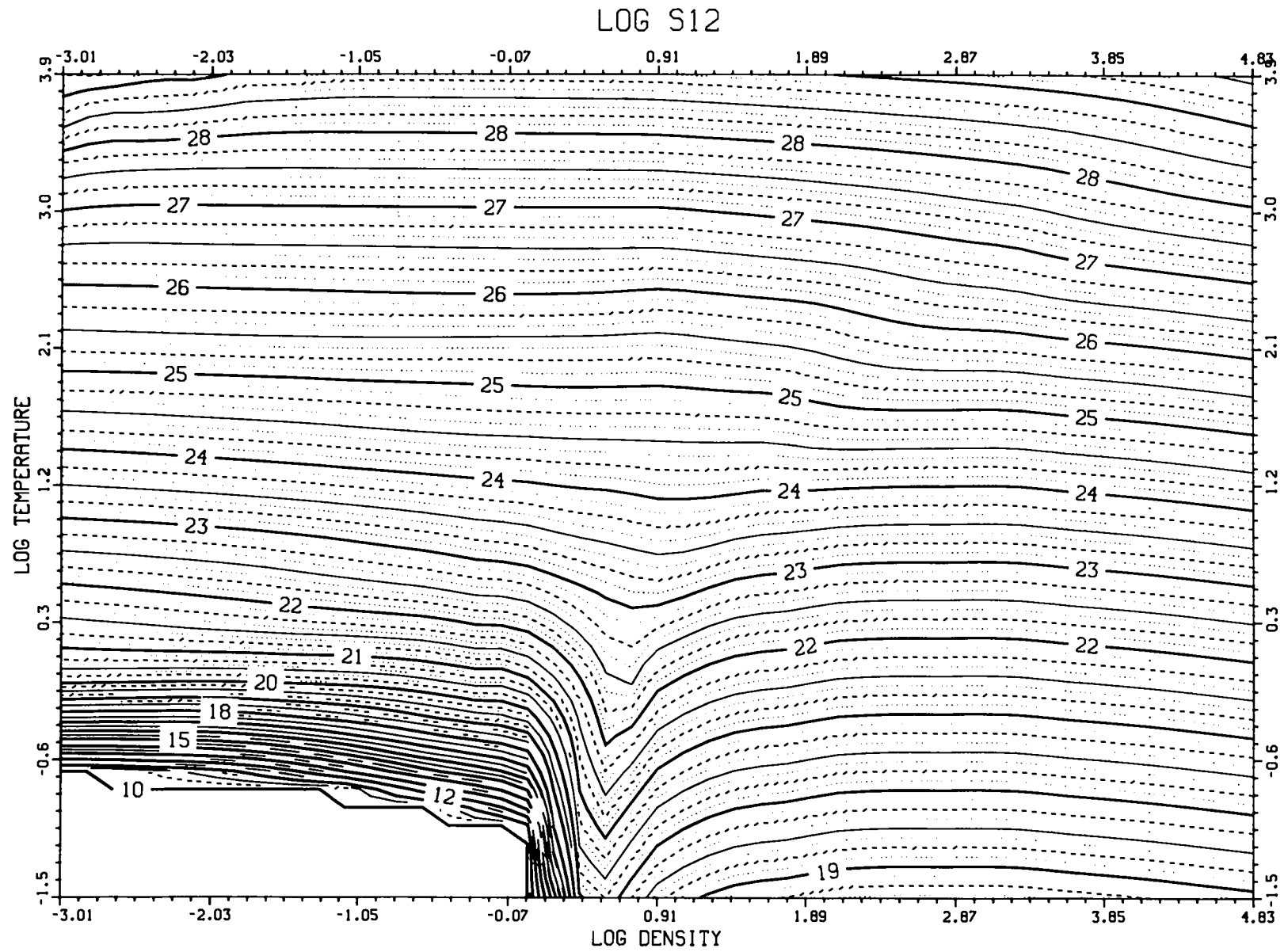


FIG. 8. Thermoelectric coefficient ($\text{cm}^{-1}\text{s}^{-1}$).

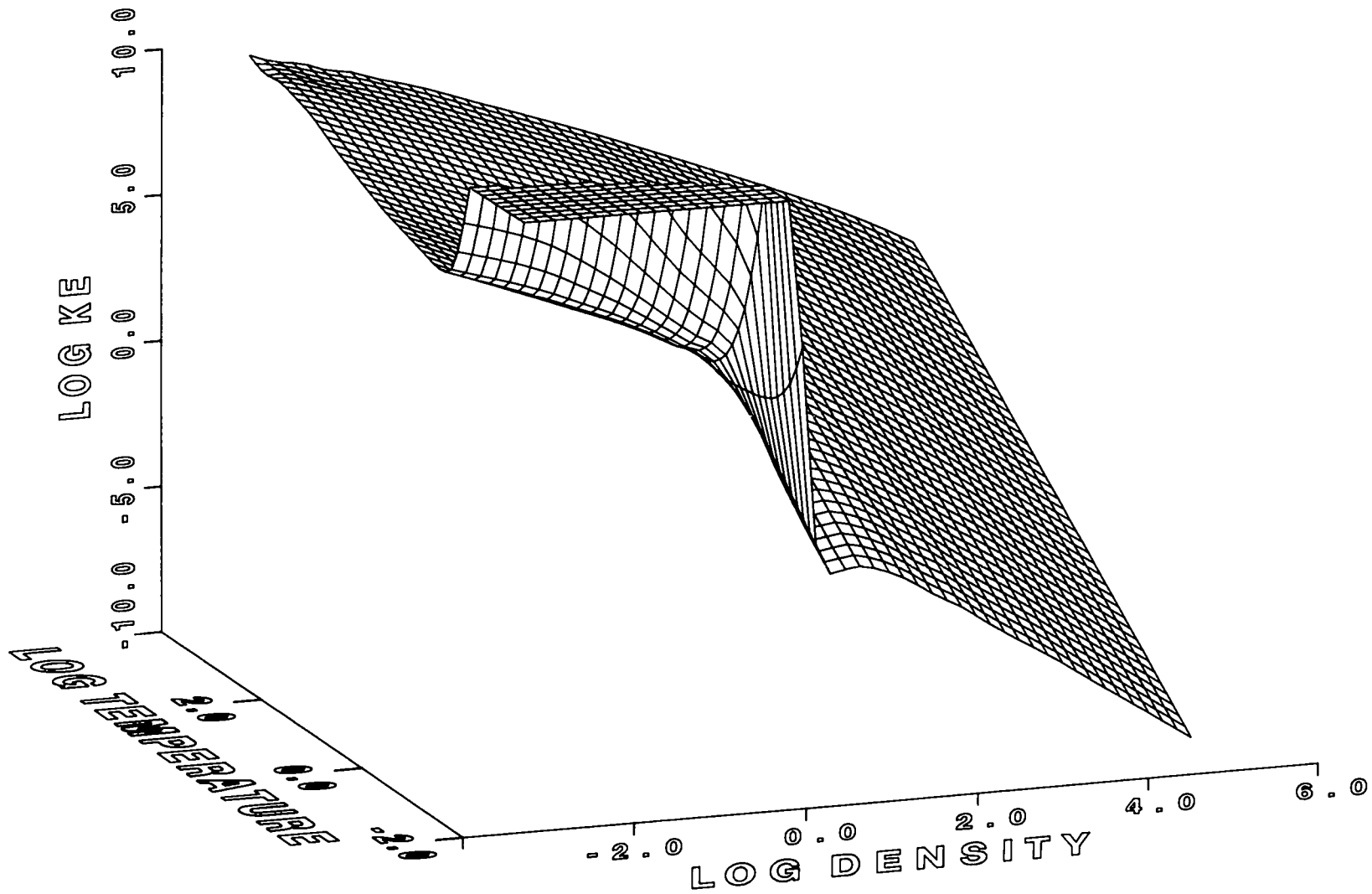


FIG. 9. Electron conductive opacity (cm^2g^{-1}).

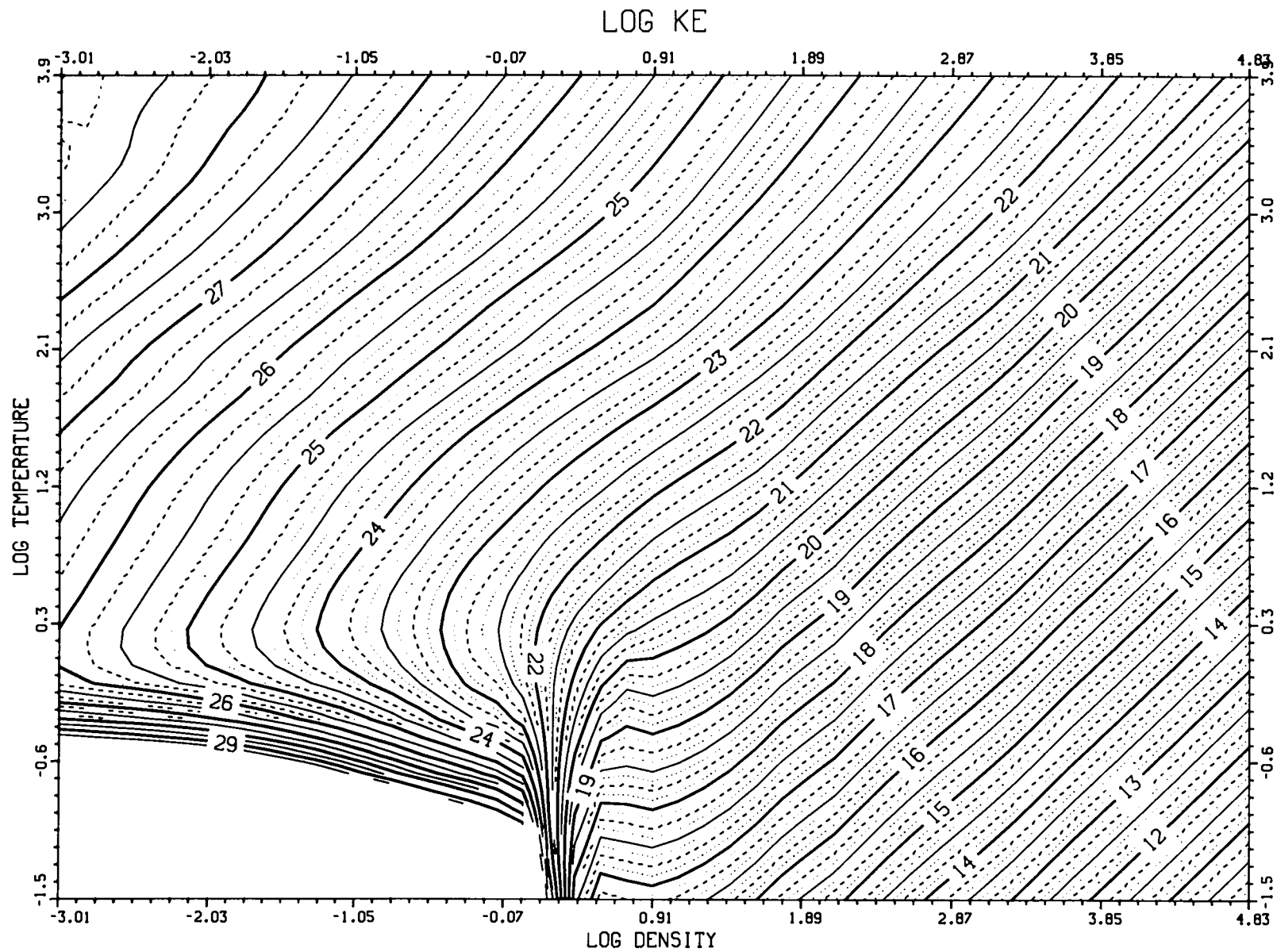


FIG. 10. Electron conductive opacity (cm^2g^{-1}).

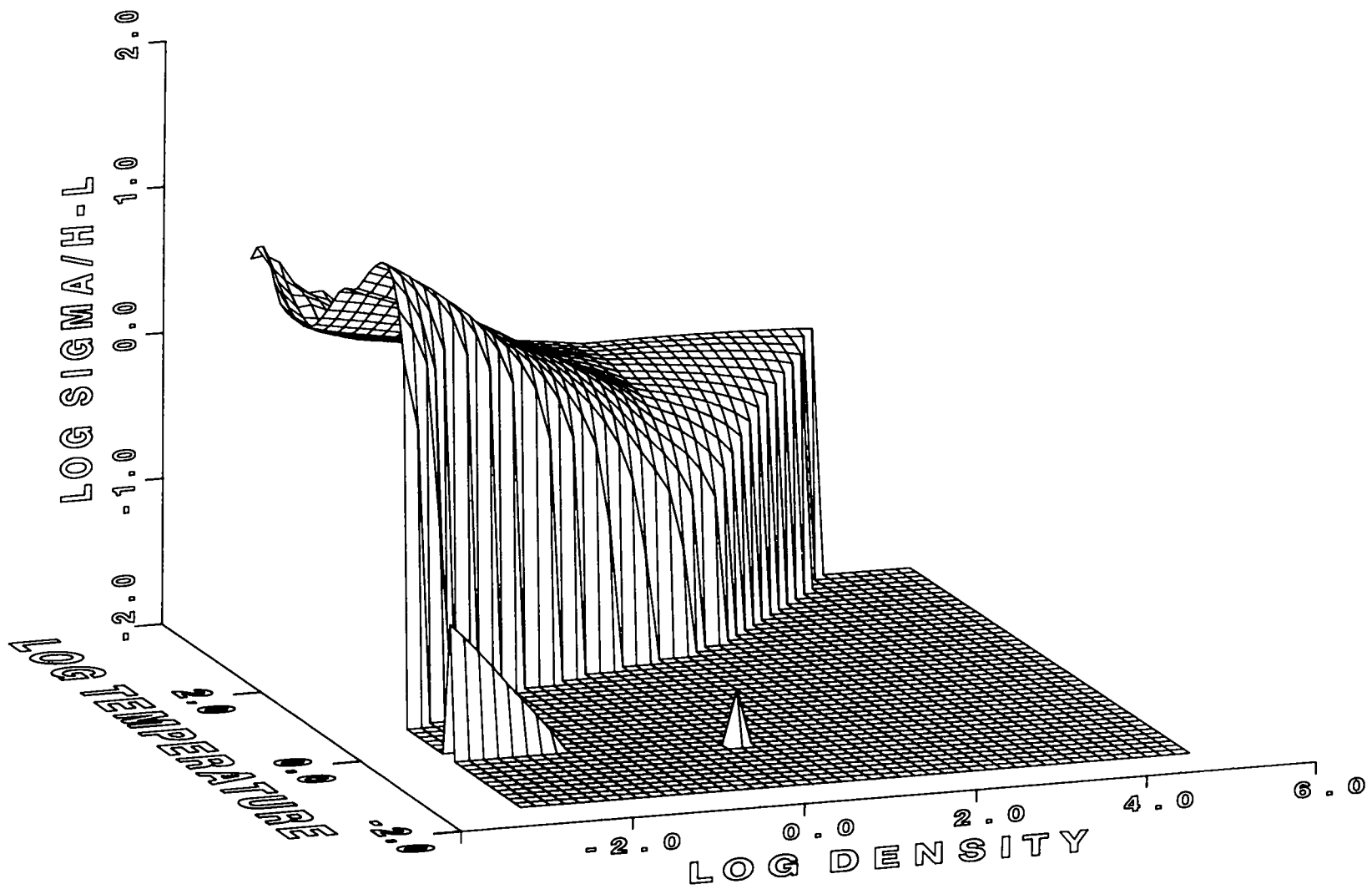


FIG. 11. Ratio of electrical conductivity to that of Hubbard and Lampe.

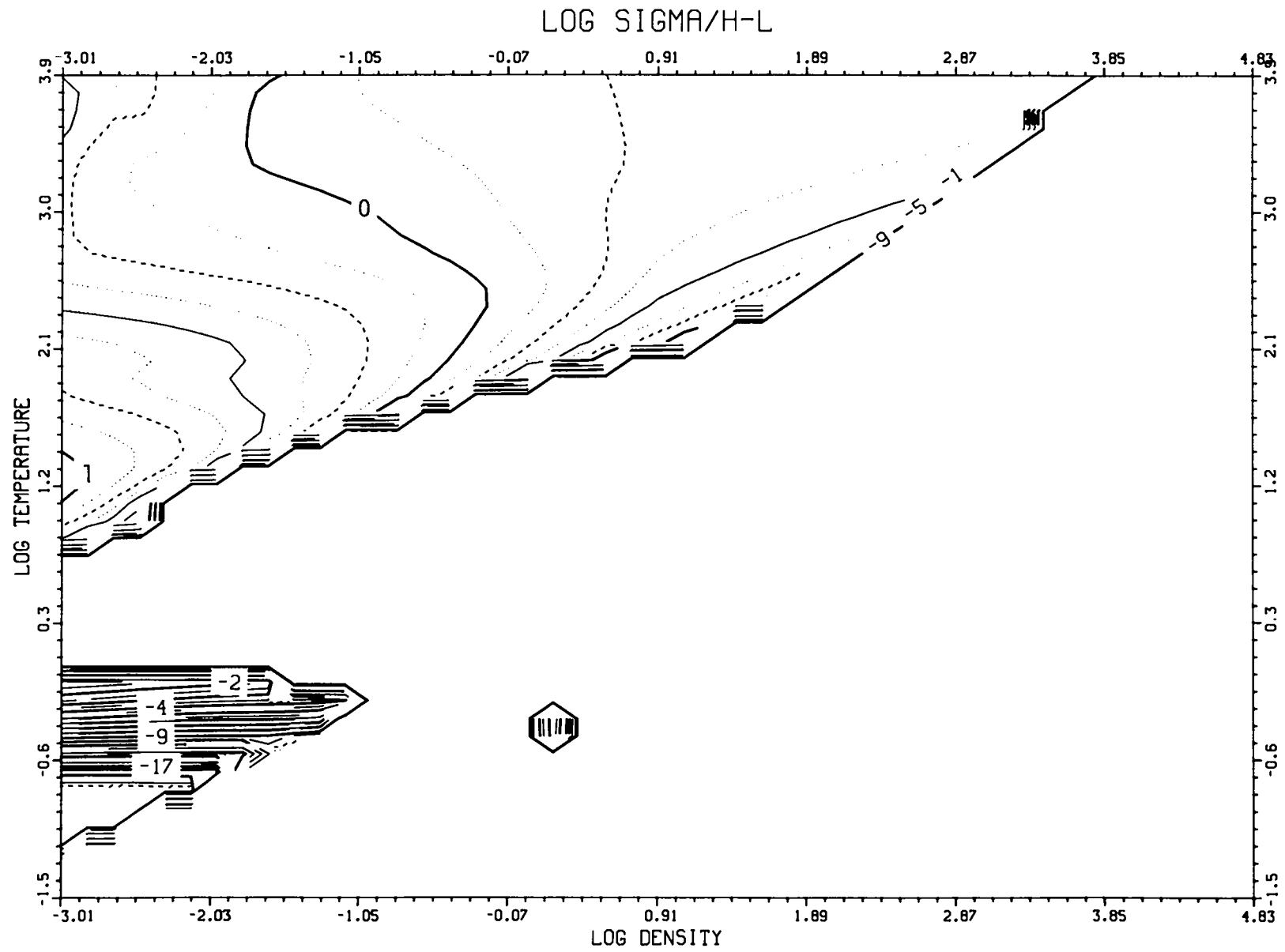


FIG. 12. Ratio of electrical conductivity to that of Hubbard and Lampe.

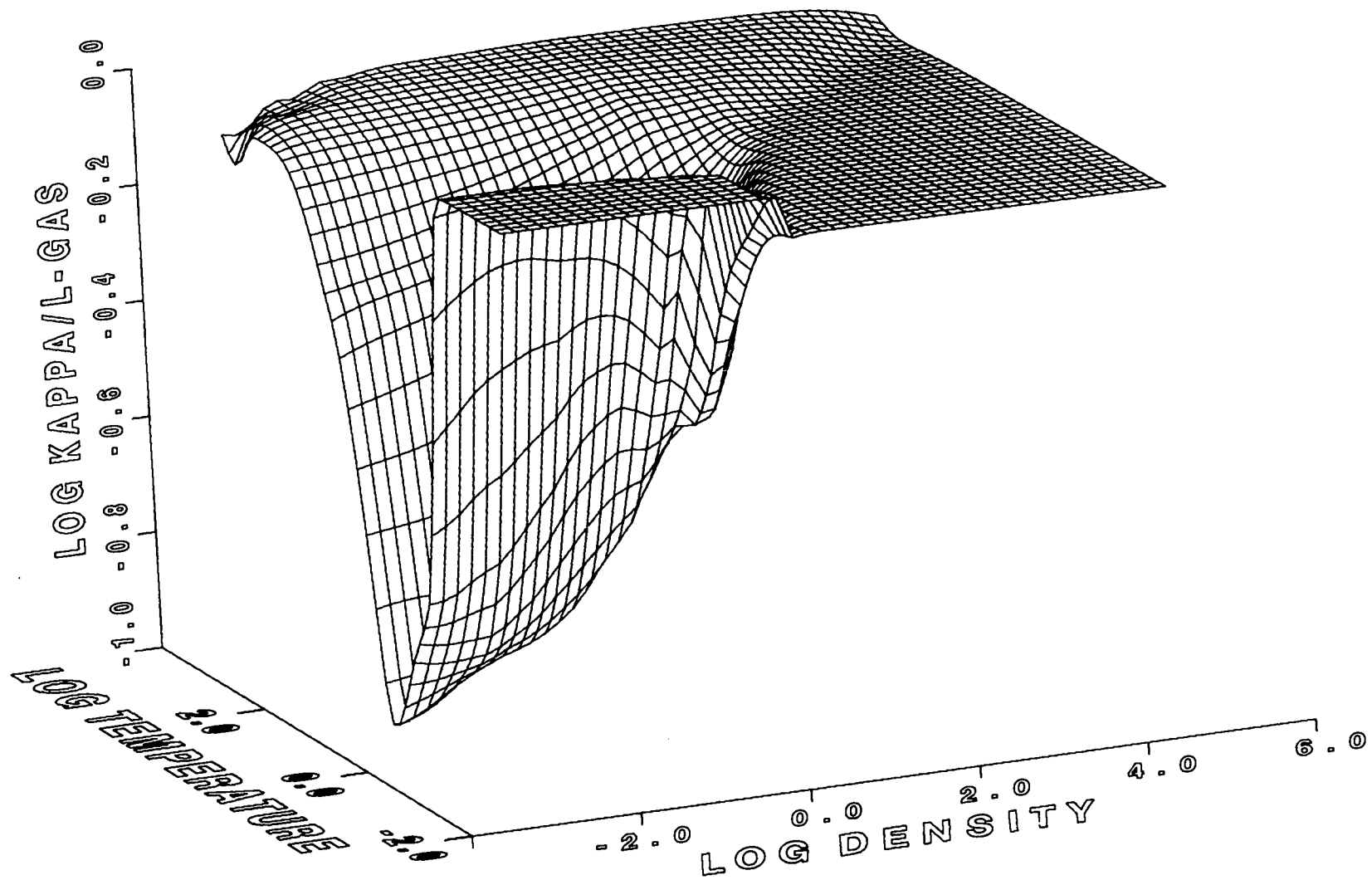


FIG. 13. Ratio of calculated thermal conductivity to the Lorentz gas model.

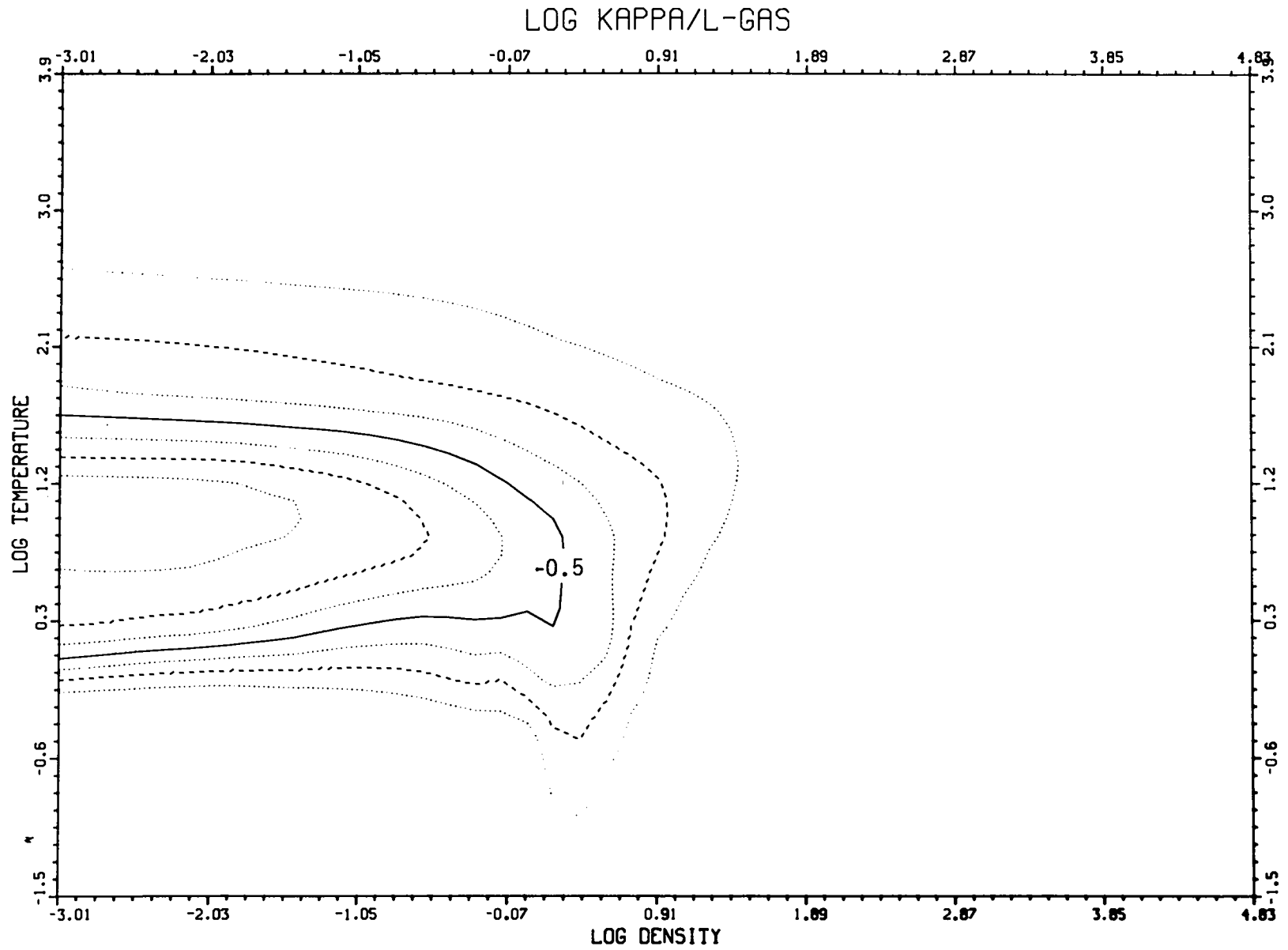


FIG. 14. Ratio of calculated thermal conductivity to the Lorentz gas model.

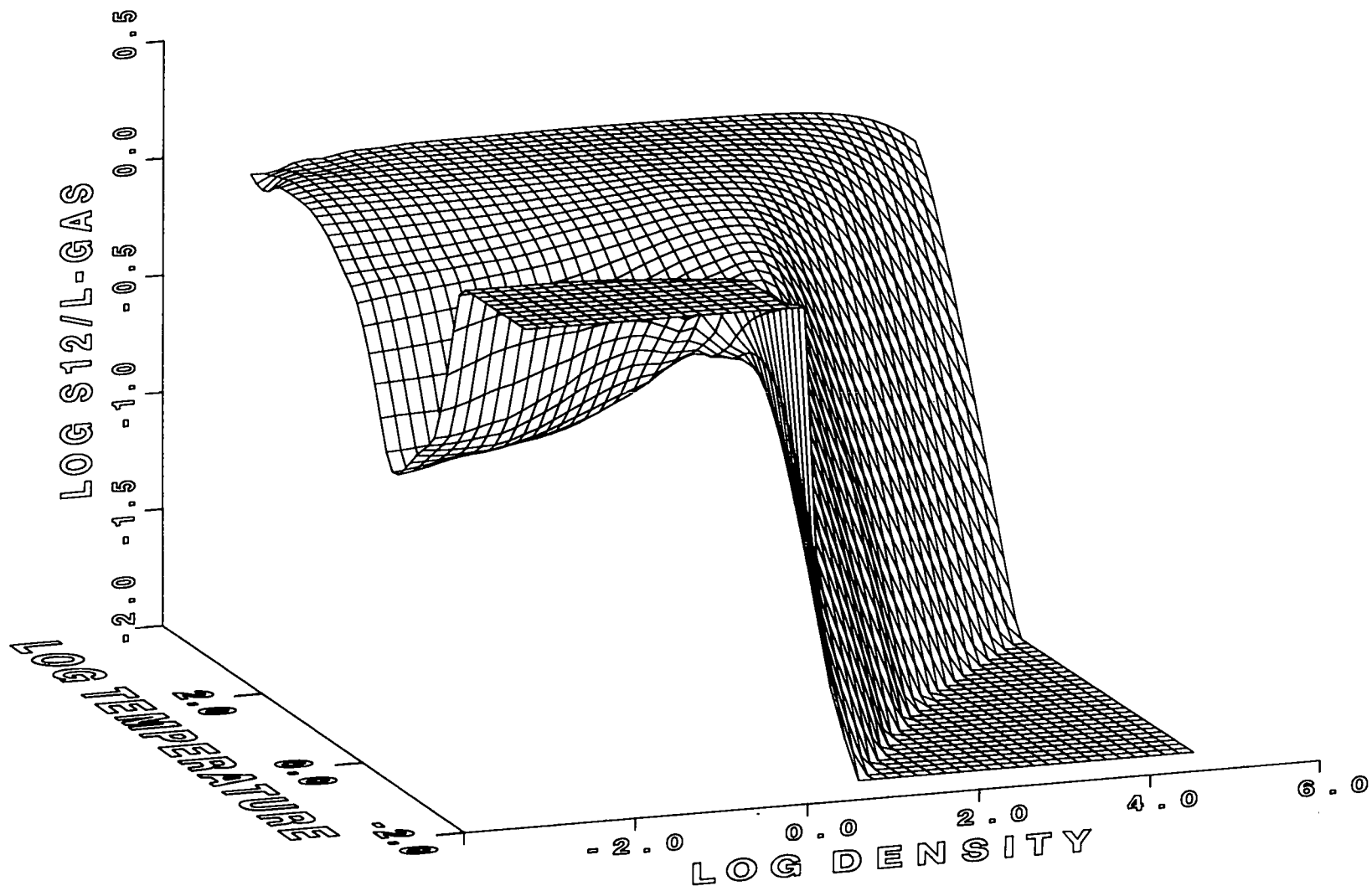


FIG. 15. Ratio of thermoelectric coefficient to the Lorentz gas model.

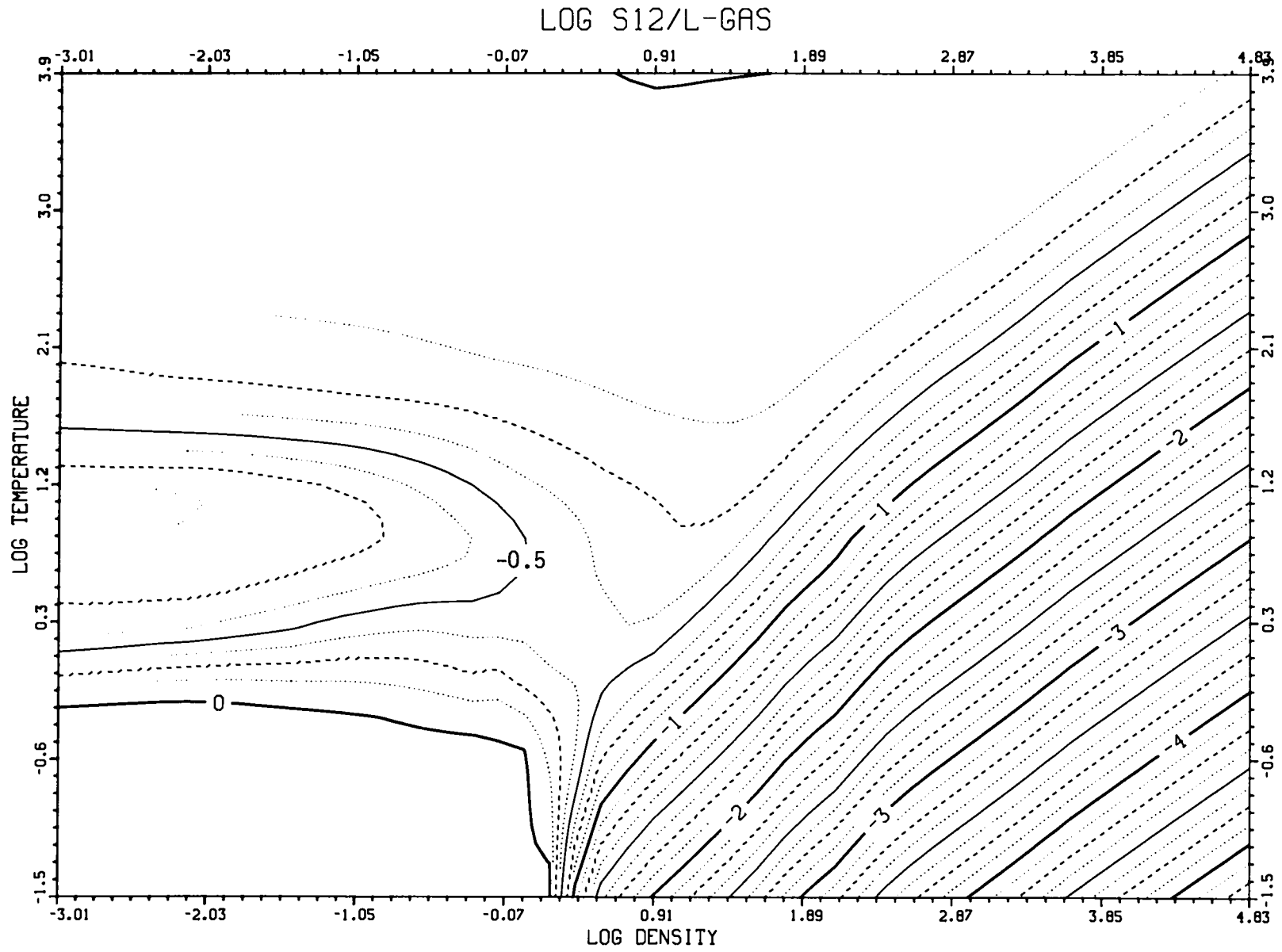


FIG. 16. Ratio of thermoelectric coefficient to the Lorentz gas model.

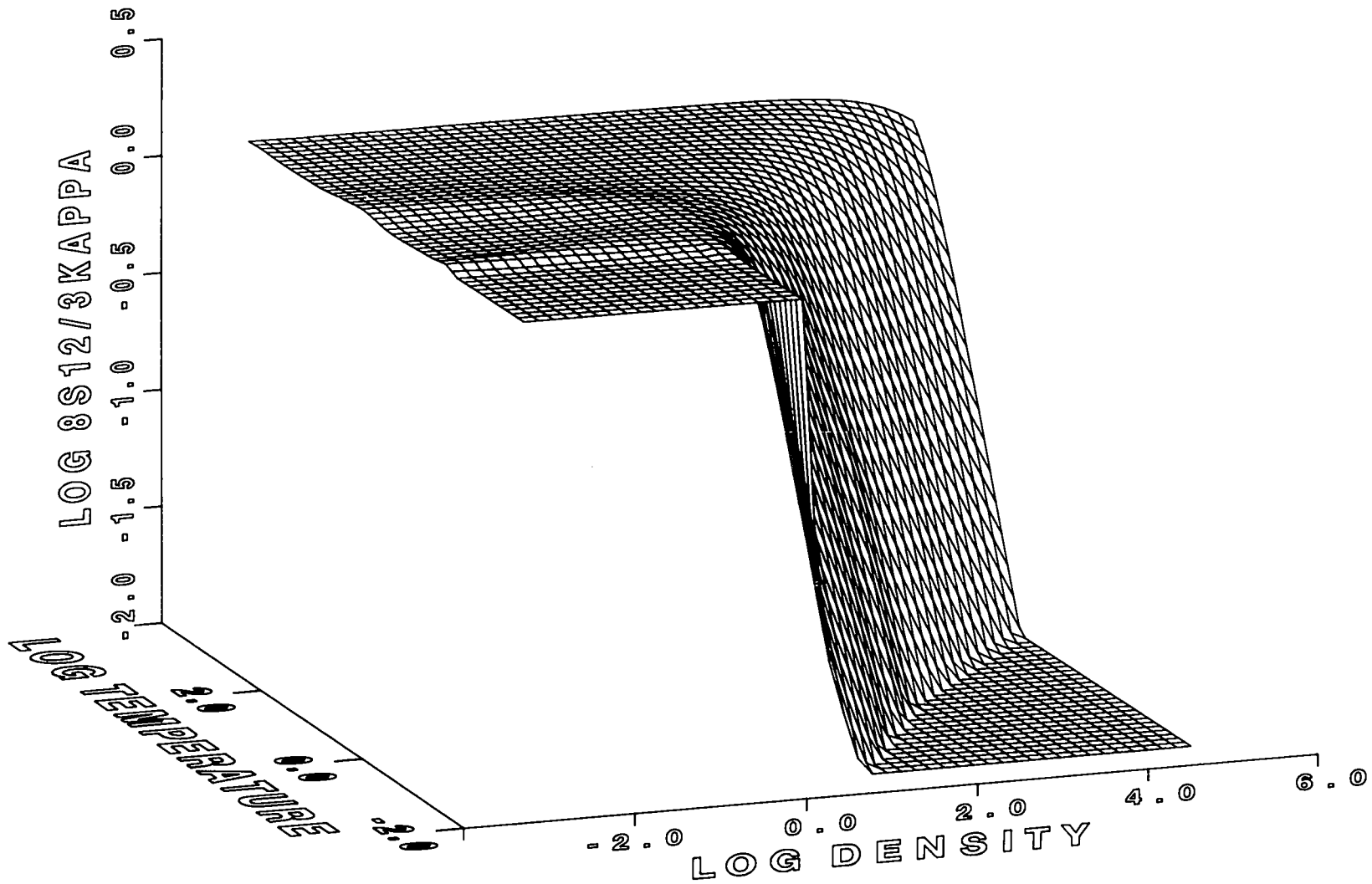


FIG. 17. Deviations from the Lorentz gas model in the ratio of thermoelectric coefficient to thermal conductivity.

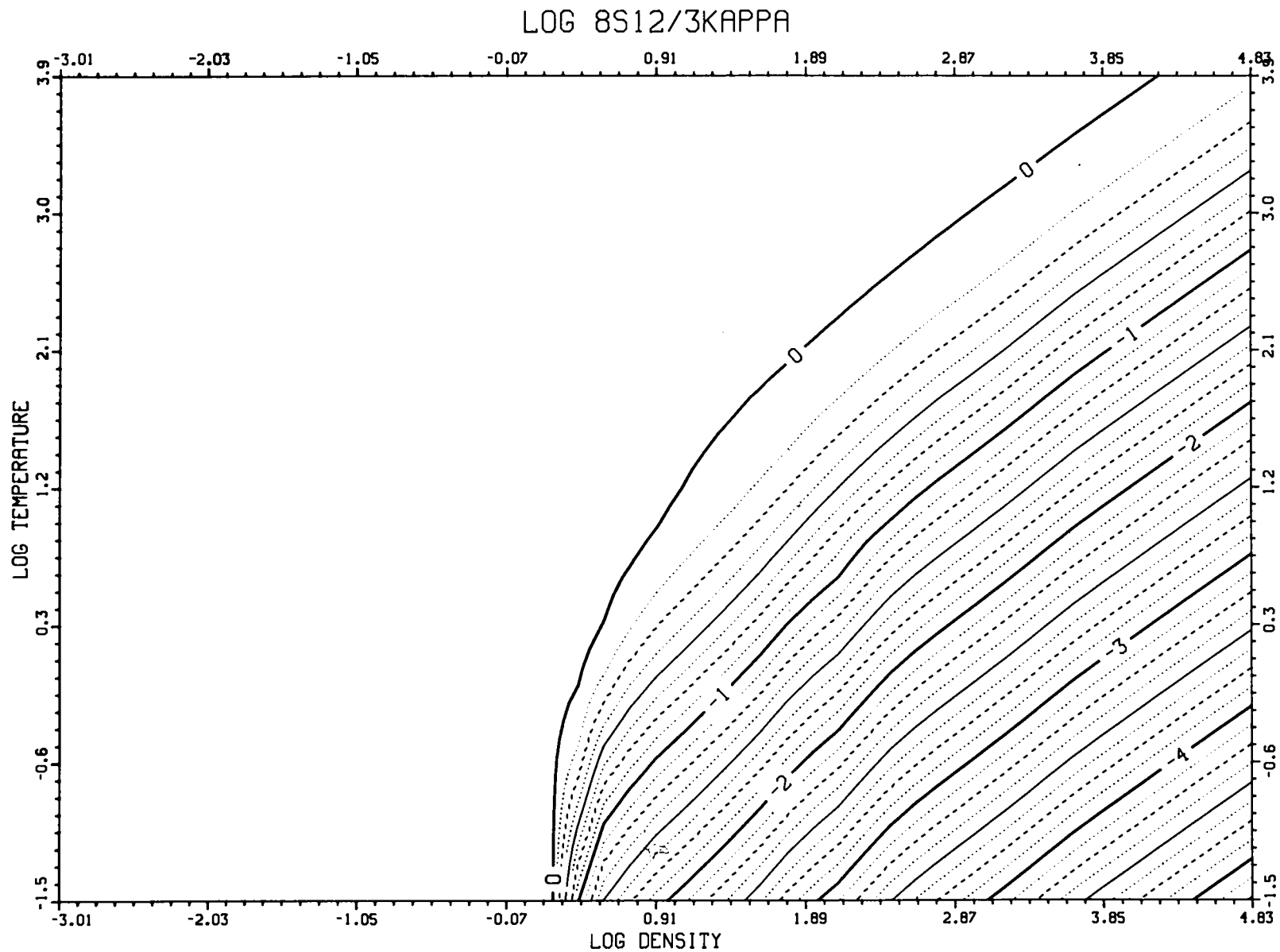


FIG. 18. Deviations from the Lorentz gas model in the ratio of thermoelectric coefficient to thermal conductivity.

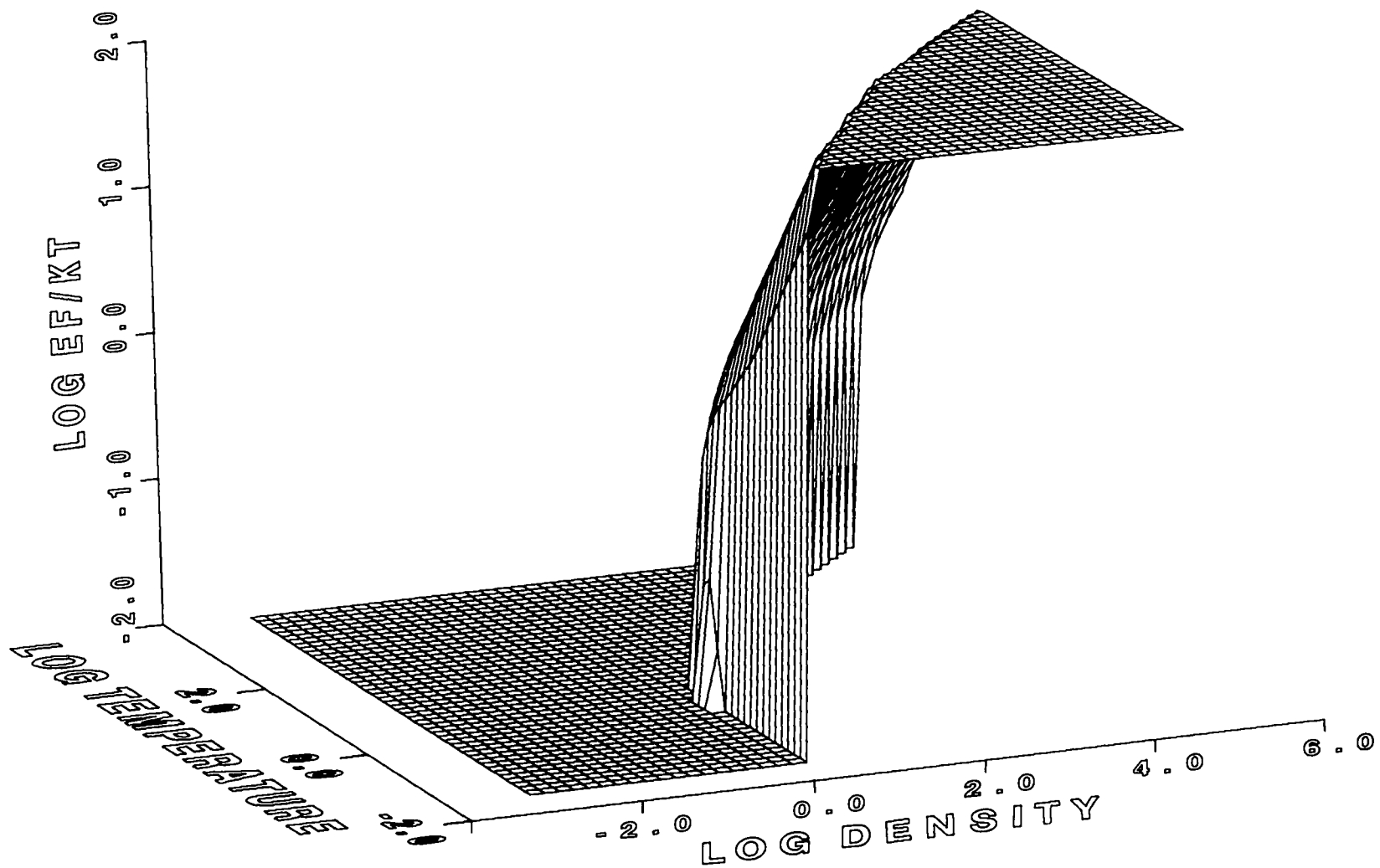
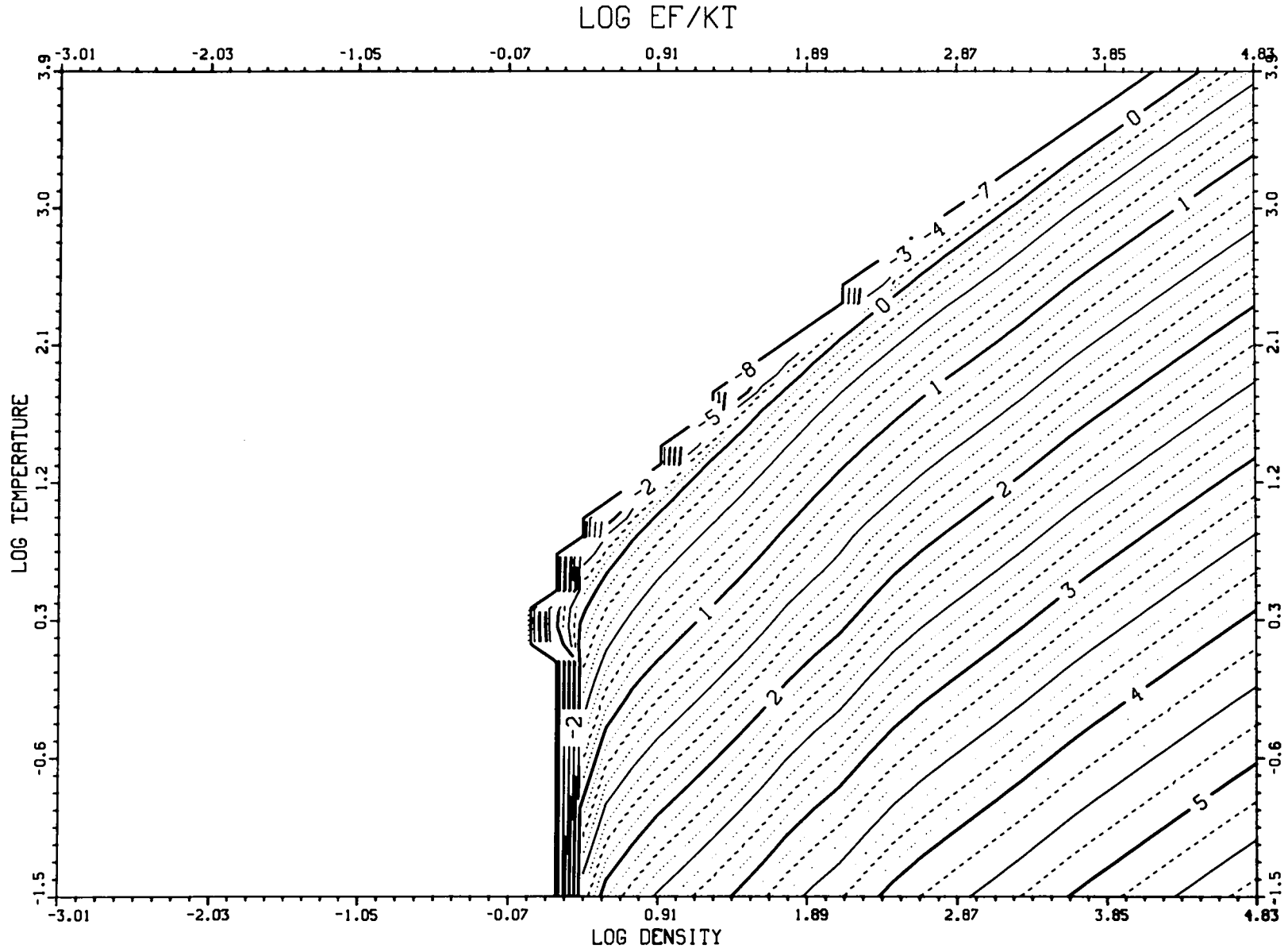


FIG. 19. Degeneracy parameter μ/kT .

FIG. 20. Degeneracy parameter μ/kT .

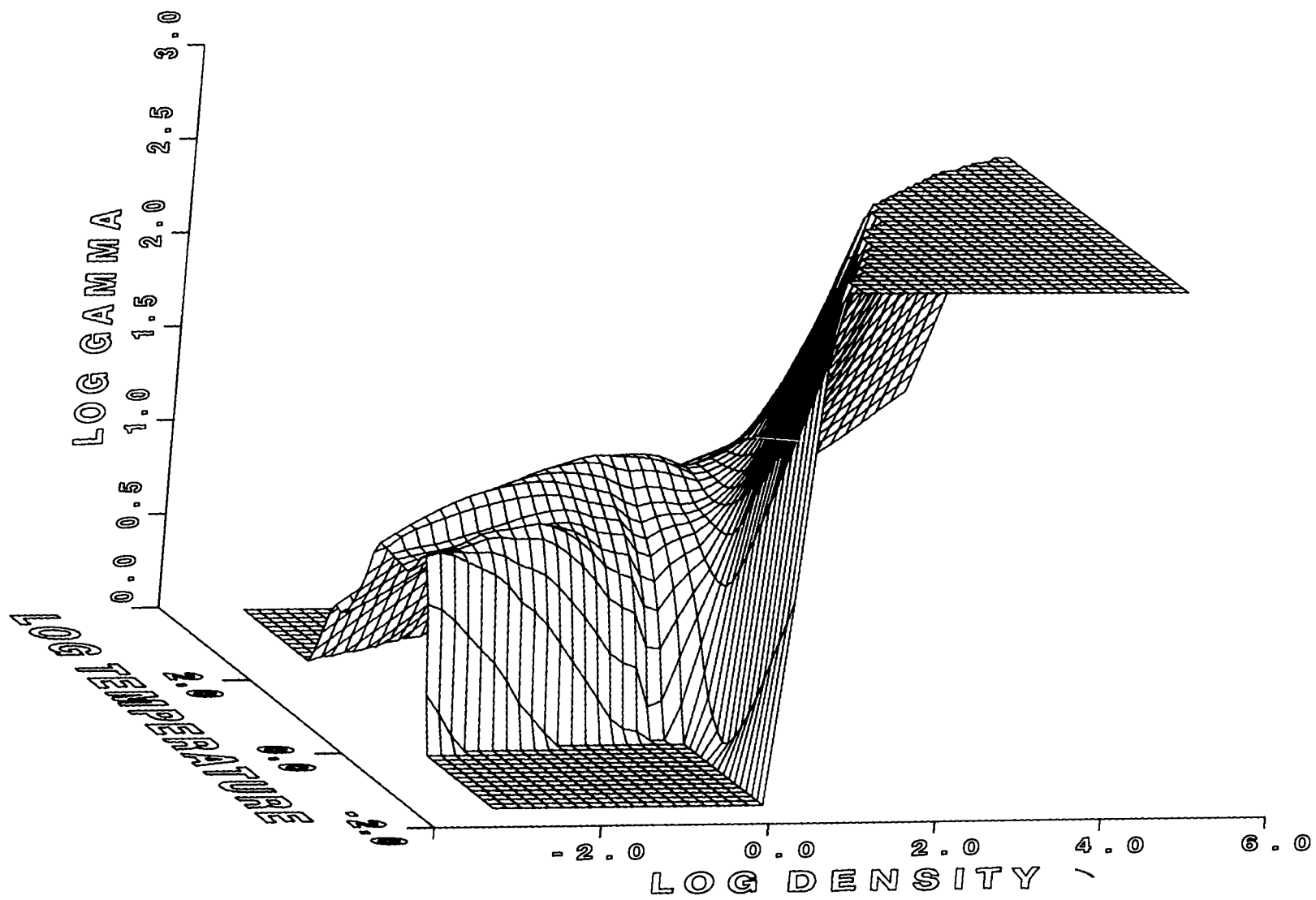
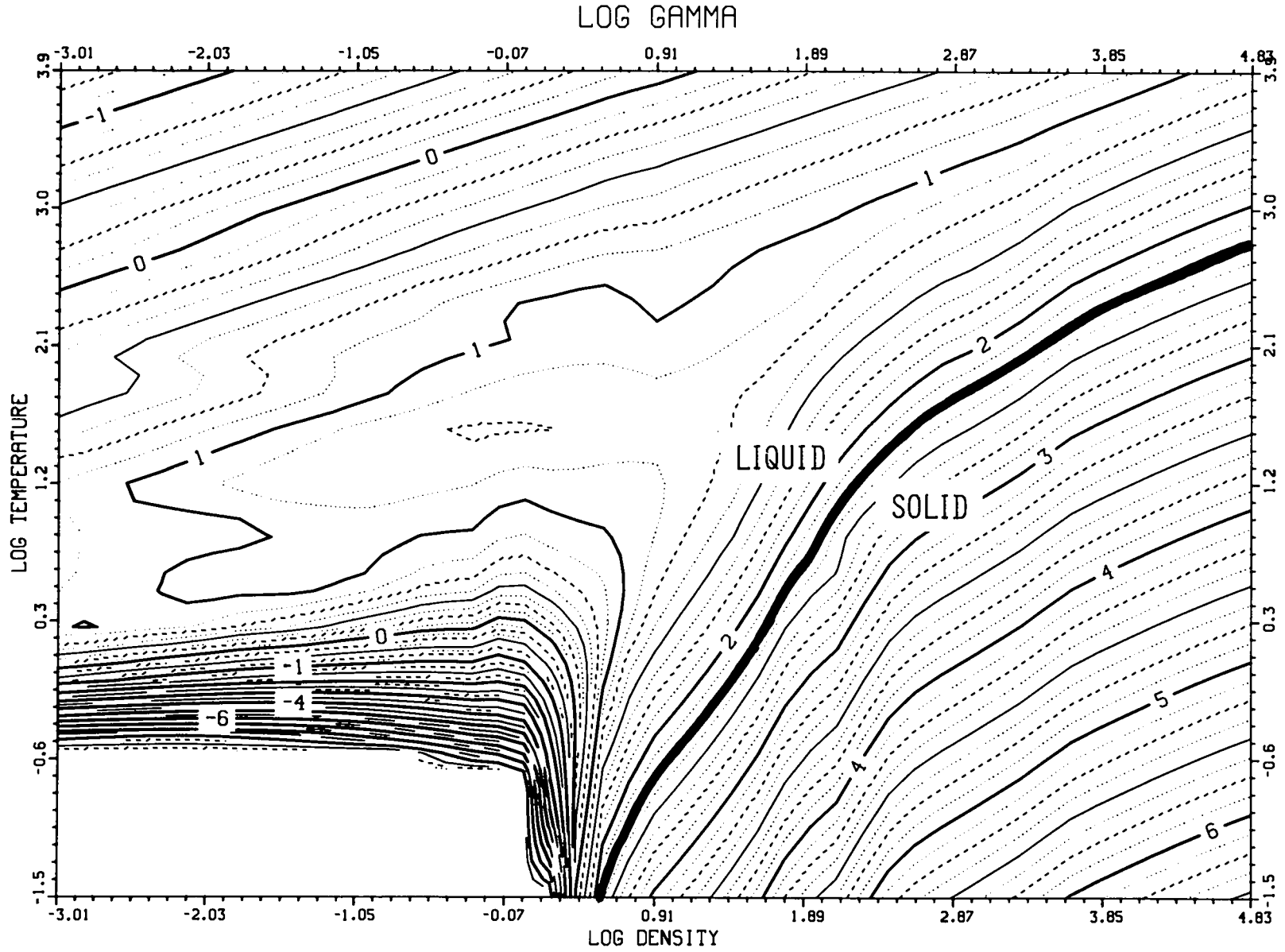


FIG. 21. Ion-ion coupling constant Γ .

FIG. 22. Ion-ion coupling constant Γ .

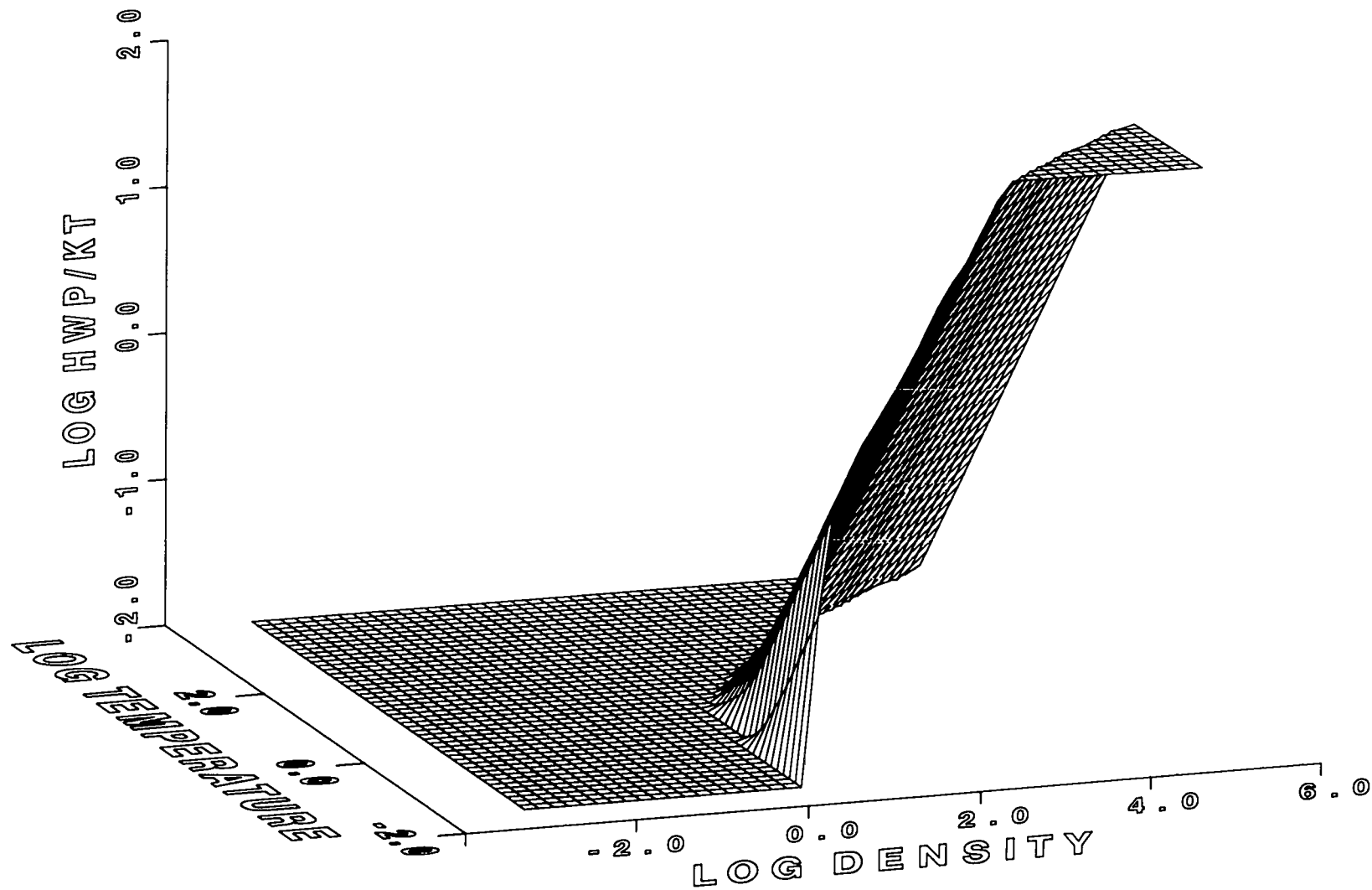
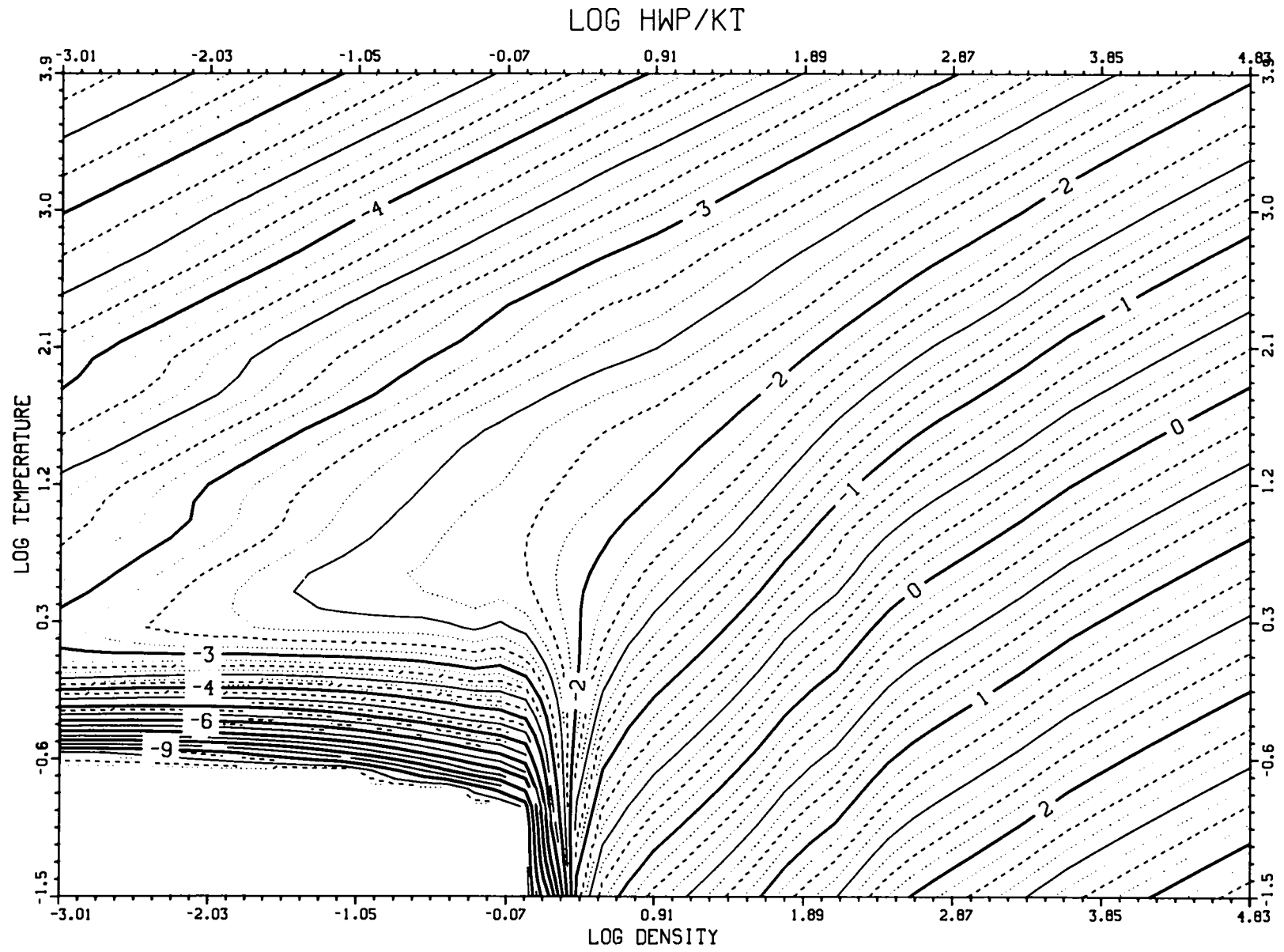


FIG. 23. Plasma frequency ω_p/kT .

FIG. 24. Plasma frequency $k\omega_p/kT$.

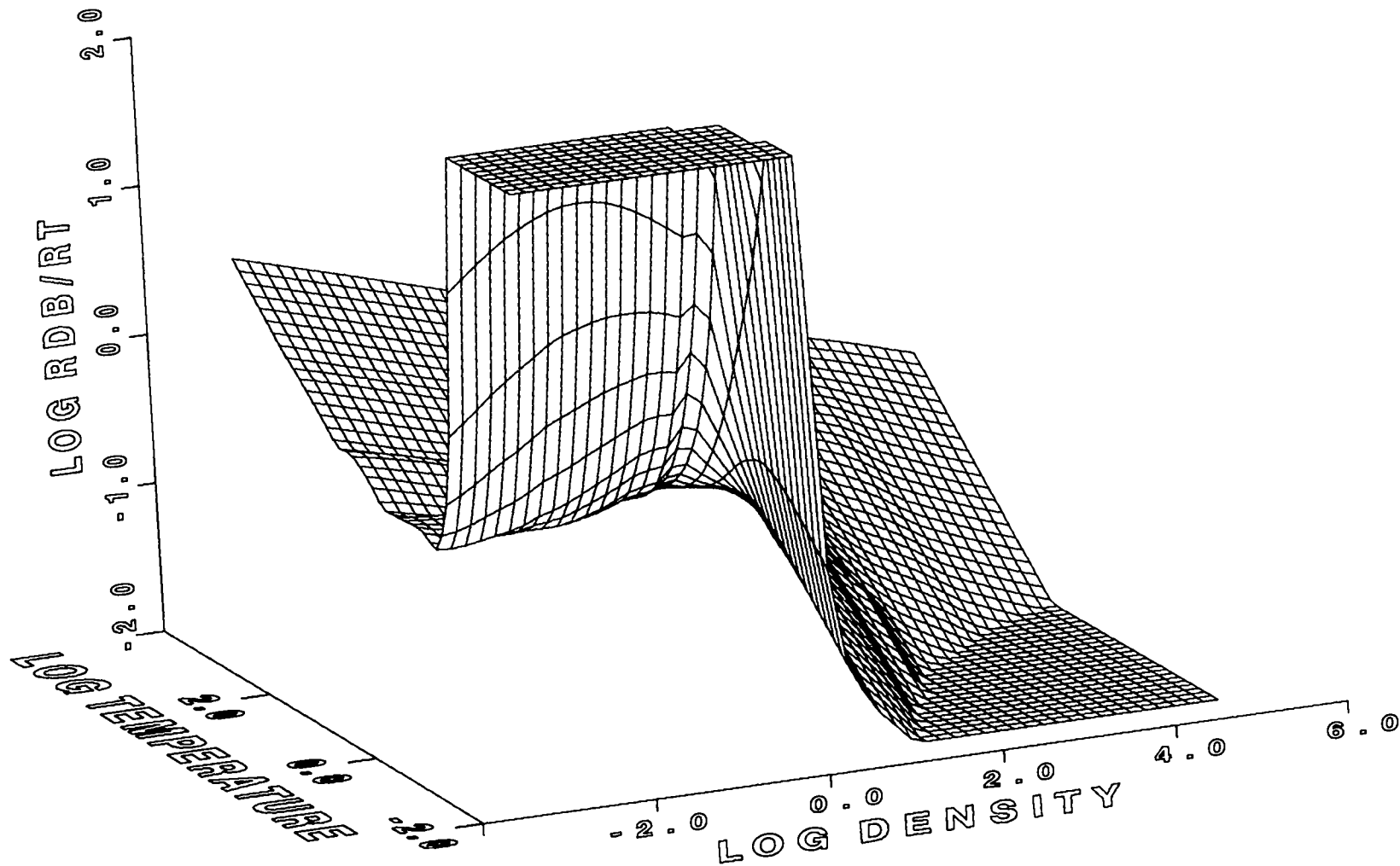
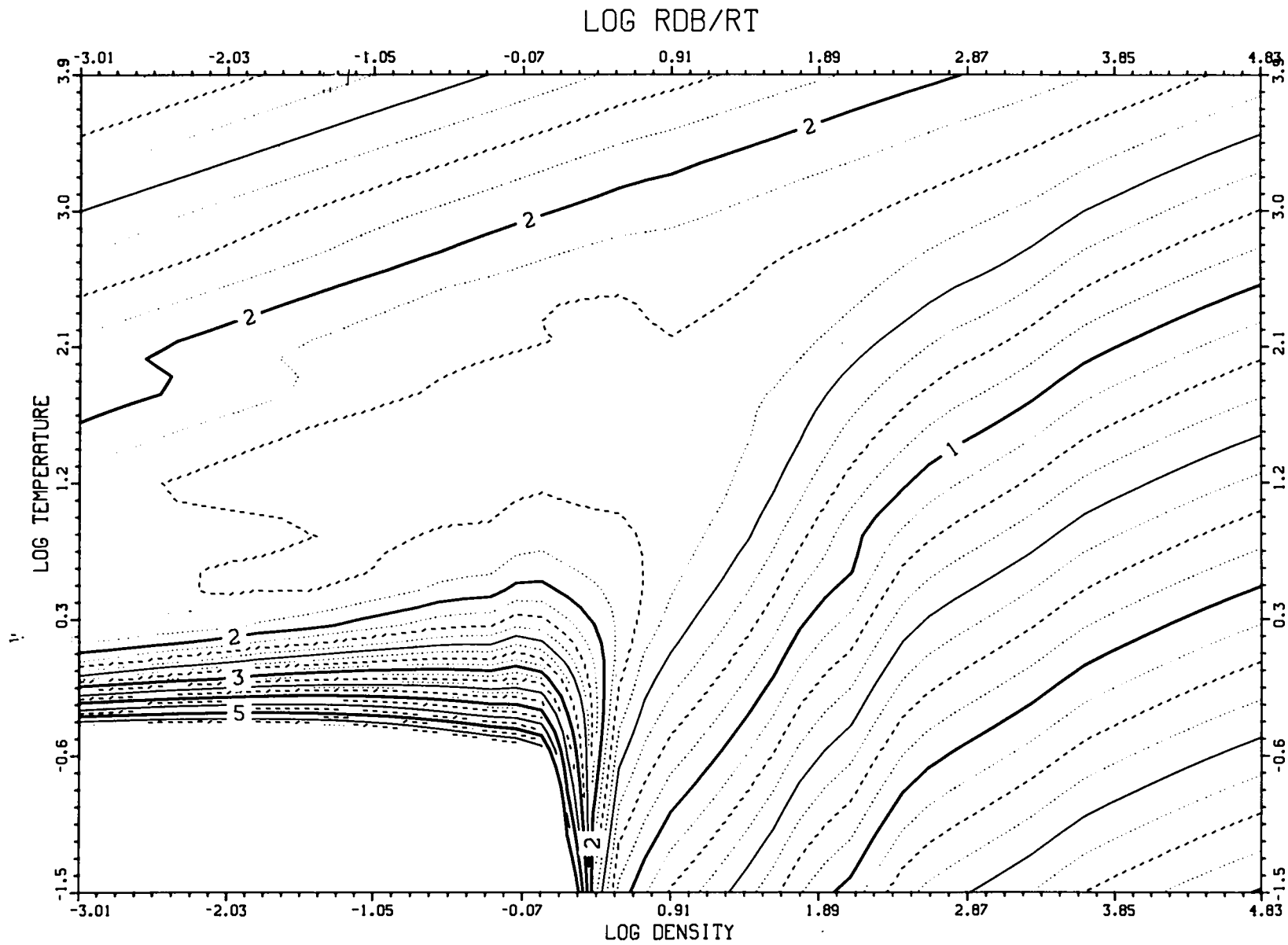


FIG. 25. Ionic Debye radius R_D/R_t .

FIG. 26. Ionic Debye radius R_D/R_t .

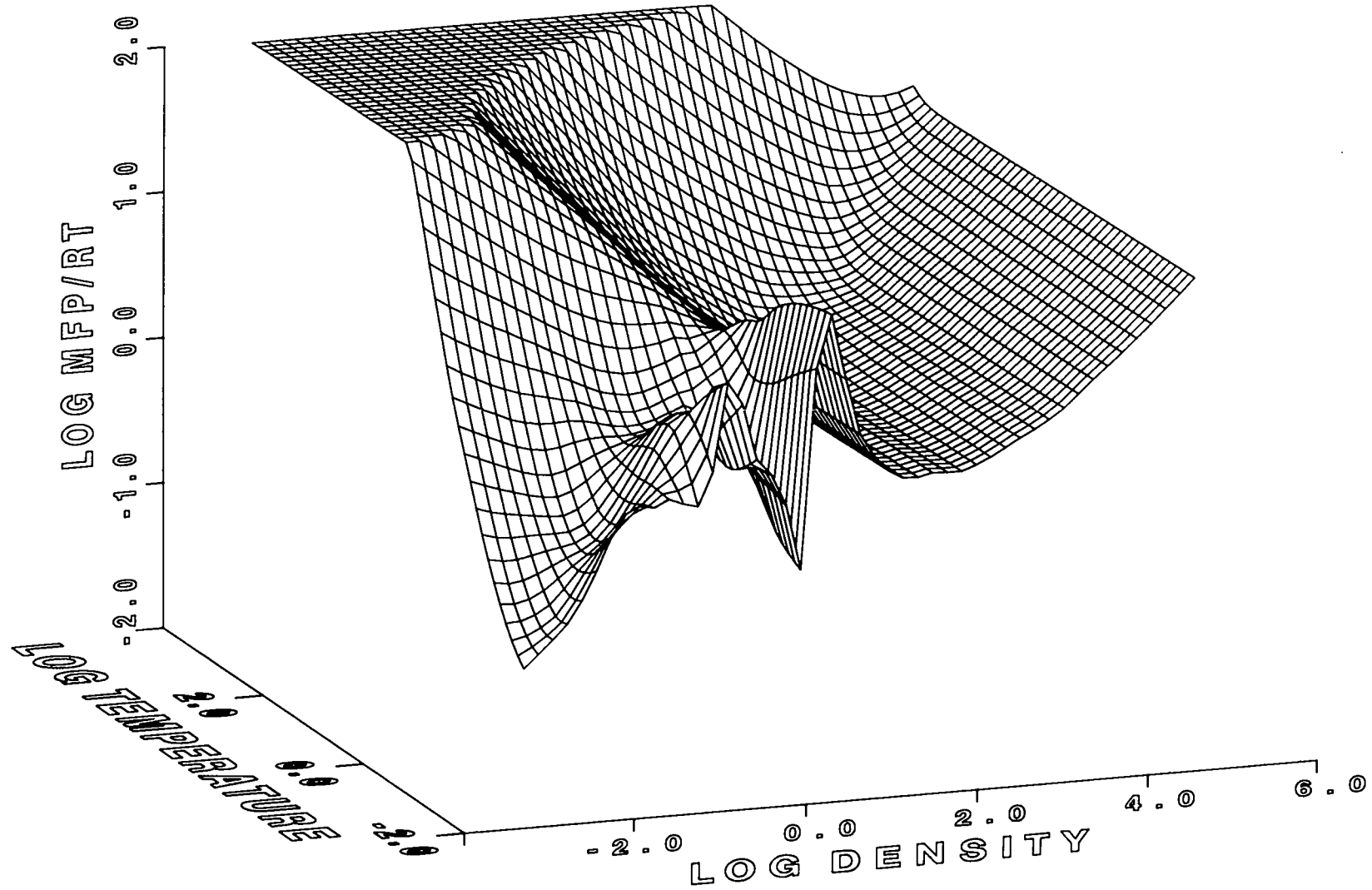
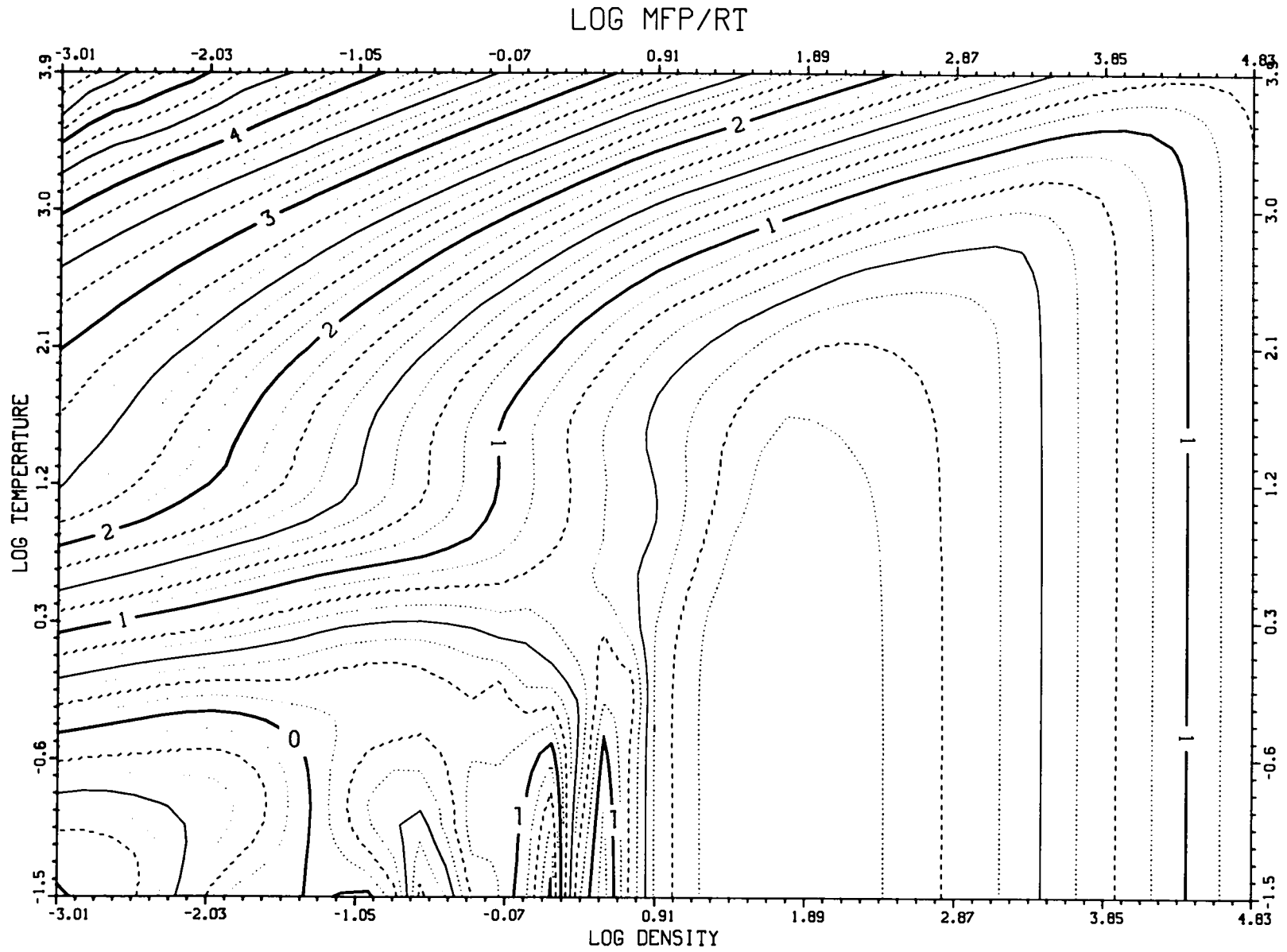


FIG. 27. Electron mean free path λ/R_t .

FIG. 28. Electron mean free path λ/R_t .

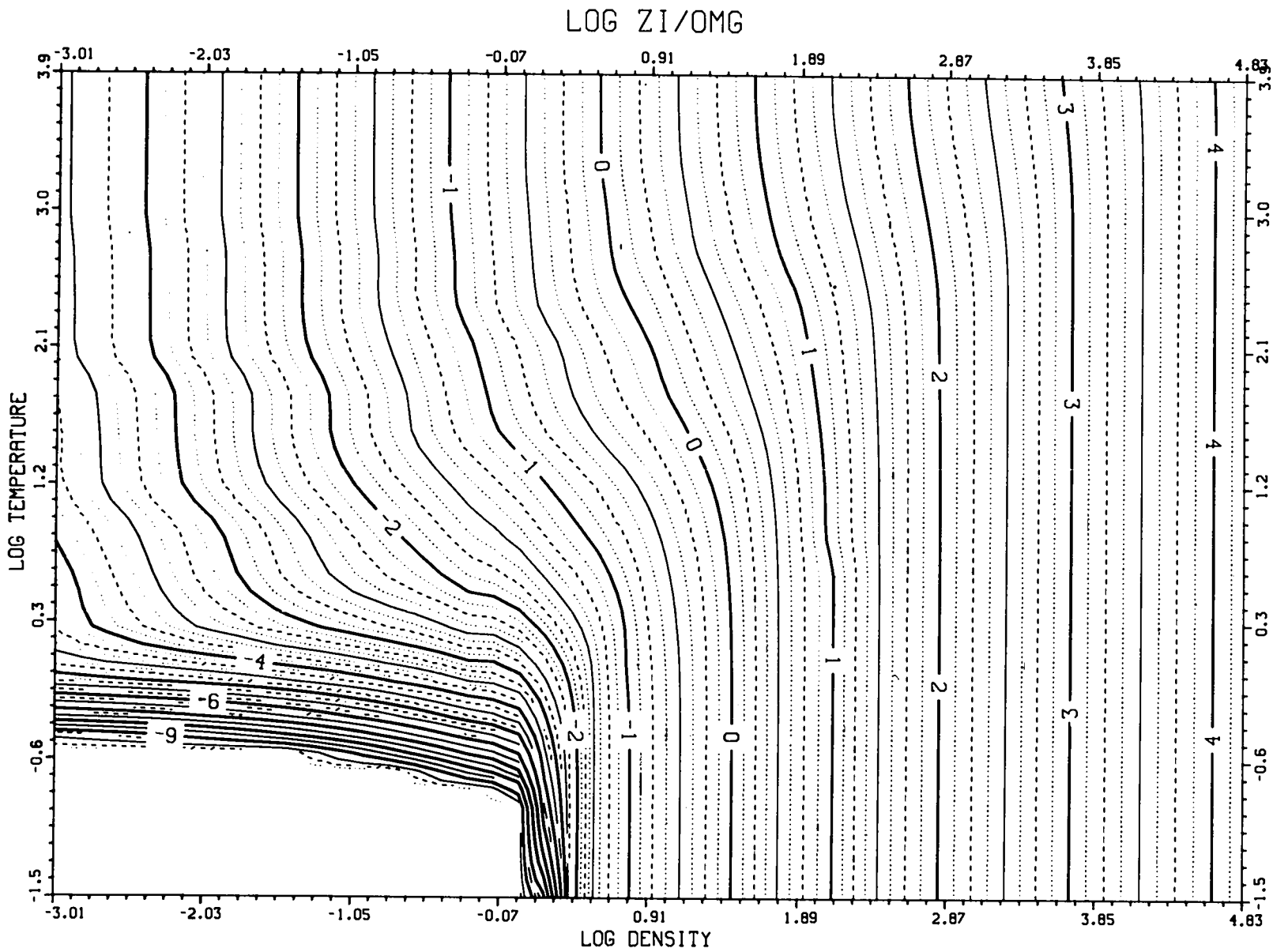


FIG. 29. Free electron number density per cubic angstrom.

Printed in the United States of America

Available from

National Technical Information Service

US Department of Commerce

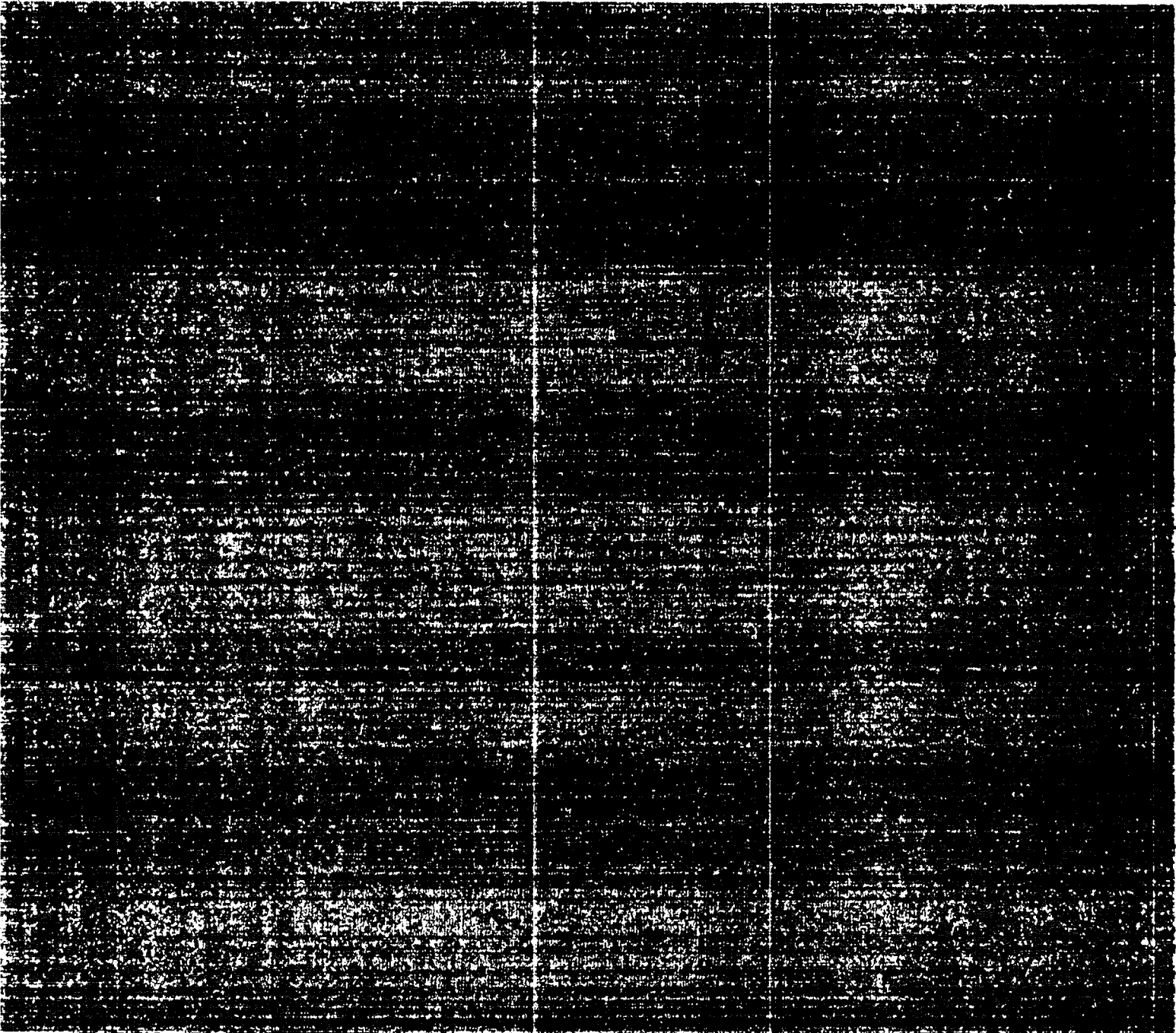
85 Port Royal Road

Springfield, VA 22161

Microfiche (A01)

NTIS		NTIS		NTIS		NTIS	
Page Range	Price Code						
007-025	A02	151-175	A08	301-325	A14	431-475	A20
026-050	A03	176-200	A09	326-350	A15	476-500	A21
051-075	A04	201-225	A10	351-375	A16	501-525	A22
076-100	A05	226-250	A11	376-400	A17	526-550	A23
101-125	A06	251-275	A12	401-425	A18	551-575	A24
126-150	A07	276-300	A13	426-450	A19	576-600	A25
						601-up*	A99

*Contact NTIS for a price quote.



Los Alamos